An Improved Convective Ice Parameterization for the NASA GISS Global Climate Model and Impacts on Cloud Ice Simulation

GREGORY S. ELSAESSER

Department of Applied Physics and Mathematics, Columbia University, and NASA Goddard Institute for Space Studies, New York, New York

ANTHONY D. DEL GENIO

NASA Goddard Institute for Space Studies, New York, New York

JONATHAN H. JIANG

Jet Propulsion Laboratory, California Institute of Technology, Pasadena, California

MARCUS VAN LIER-WALQUI

NASA Goddard Institute for Space Studies, and Center for Climate Systems Research, Columbia University, New York, New York

ABSTRACT

Partitioning of convective ice into precipitating and detrained condensate presents a challenge for GCMs since partitioning depends on the strength and microphysics of the convective updraft. It is an important issue because detrainment of ice from updrafts influences the development of stratiform anvils, impacts radiation, and can affect GCM climate sensitivity. Recent studies have shown that the CMIP5 configurations of the Goddard Institute for Space Studies (GISS) GCM simulated upper-tropospheric ice water content (IWC) that exceeded an estimated upper bound by a factor of 2. Partly in response to this bias, a new GCM parameterization of convective cloud ice has been developed that incorporates new ice particle fall speeds and convective outflow particle size distributions (PSDs) from the NASA African Monsoon Multidisciplinary Analyses (NAMMA), NASA Tropical Composition, Cloud and Climate Coupling (TC4), DOE ARM–NASA Midlatitude Continental Convective Clouds Experiment (MC3E), and DOE ARM Small Particles in Cirrus (SPARTICUS) field campaigns. The new parameterization assumes a normalized gamma PSD with two novel developments: no explicit assumption for particle habit in the calculation of mass distributions, and a formulation for translating ice particle fall speeds as a function of maximum diameter into fall speeds as a function of melted-equivalent diameter. Two parameters (particle volume– and projected area–weighted equivalent diameter) are diagnosed as a function of temperature and IWC in the convective plume, and these parameters constrain the shape and scale of the normalized gamma PSD. The diagnosed fall speeds and PSDs are combined with the GCM's parameterized convective updraft vertical velocity to partition convective updraft condensate into precipitating and detrained components. A 5-yr prescribed sea surface temperature GCM simulation shows a 30%–50% decrease in upper-tropospheric deep convective IWC, bringing the tropical and global mean ice water path into closer agreement with *CloudSat* best estimates.

Corresponding author address: Gregory S. Elsaesser, Department of Applied Physics and Applied Mathematics, Columbia University, and NASA Goddard Institute for Space Studies, 2880 Broadway, New York, NY 10025.
E-mail: gregory.elsaesser@columbia.edu

1. Introduction

Upper-tropospheric ice clouds, often produced from large-scale, deep-tropospheric lifting or via detrainment of cloud ice from deep convective plumes, can strongly

influence Earth's climate given their impact on radiation fields (Stephens 2005; Bony et al. 2006). Ice cloud thickness, height, and microphysical properties (e.g., particle shapes and sizes) impact both shortwave and longwave radiation components (Hartmann et al. 1992; Zelinka et al. 2012a,b). Therefore, quantifying and simulating ice cloud properties is a continuing goal to be met so that accurate understanding of cloud feedbacks and modeling of Earth's climate sensitivity is achieved (Sanderson et al. 2008; Zhao 2014; Bony et al. 2015).

Particularly in the midlatitudes and tropics, expansive fields of ice clouds, resulting from the detrainment of cloud ice in deep convection (Luo and Rossow 2004), are the end result of processes that influence convective updraft vertical velocities, convective areal fractions (which are also influenced by convective organization), ice particle size distributions (PSDs), and ice particle fall velocities. While some benchmarks exist for validating these properties, historically, quantifying these components in deep convection from in situ observations or remote sensing methods has proven difficult (Comstock et al. 2007). For instance, from an in situ perspective, for safety reasons, aircraft are unable to fly and sample the most vigorous deep convective updrafts (G. Heymsfield et al. 2010). Additionally, remote sensing retrievals often rely on radiation that either is unable to penetrate the deepest convective clouds (i.e., shorter-wavelength radiation) or is attenuated as a result of substantial condensate. The use of microwave wavelengths partly evades this latter issue (e.g., Evans and Stephens 1995; Evans et al. 2005), but the deepest cores still attenuate radiation. The historical lack of observations may in part be responsible for the substantial diversity in past global climate model (GCM)-simulated ice water content (IWC) and ice water path (IWP) fields.

Some GCMs have experimented with sophisticated microphysics parameterizations for convective updrafts (e.g., Song and Zhang 2011; Storer et al. 2015). However, sparsely validated remote sensing products and lack of formulations for parameterizing convective updraft velocities, the latter of which is required for performing physical partitioning of updraft IWC, has motivated the use of simple precipitation efficiency assumptions, IWC thresholds, cloud water fluxes, or pressure- or temperature-dependent autoconversion rates for precipitation onset in most operational GCM parameterizations (Zhang and McFarlane 1995; Emanuel and Živković-Rothman 1999; Clement and Soden 2005; Mauritsen and Stevens 2015). While this simplicity is appealing, such a partitioning approach may be inflexible to the point that

systematically changing convection strength and ice particle properties in a warming climate may render such a parameterization less useful for simulating cloud feedbacks, as it is less certain that realistic partitioning can be performed in climate change simulations whose models employ simple autoconversion functions (Rotstayn 2000).

Over the last 10–20 years, IWC retrieval algorithms for satellites such as *CloudSat* (Stephens et al. 2002) and *Aura* EOS MLS (Waters et al. 2006) have matured enough to provide good benchmarks for global IWC properties (Waliser et al. 2009). Over this same period, a diverse number of field programs and satellite intercomparison studies have provided validation for satellite estimates (Wu et al. 2008, 2009; Protat et al. 2010) as well as additional useful in situ derived ice cloud characteristics pertaining to PSDs and shapes, among other properties (e.g., Heymsfield et al. 2002; McFarquhar et al. 2007; A. Heymsfield et al. 2010, 2013; Jackson et al. 2015; Fridlind et al. 2015). Furthermore, GCM convective parameterizations have begun to include a formulation for subgrid-scale average convective vertical velocity (e.g., Donner et al. 2001; Del Genio et al. 2007). A focus on diagnosing convective vertical velocities is expected to continue (Donner et al. 2001, 2011), particularly since vertical velocities are both integral to aerosol activation and vital to convective microphysics. Surface-based retrievals of convective updraft speeds from Doppler radars and radar wind profilers are beginning to provide constraints for such parameterizations (Collis et al. 2013; Giangrande et al. 2013).

The GISS Model E2 is among those GCMs that parameterize updraft vertical velocity, thus allowing for a more physical ice mass partitioning scheme to be used. With respect to the treatment of the less-dense ice species, prior to now, an exponential Marshall–Palmer (M-P) PSD (Marshall and Palmer 1948) has been assumed to separate convective updraft cloud from precipitating ice [with a constant intercept parameter $(8 \times 10^6 \, \mathrm{m}^{-4})$]. Particles were assumed to be spherical with nonvarying densities $(100 \, \mathrm{kg \, m}^{-3})$. Particle terminal velocities were fixed, most recently according to the Locatelli and Hobbs (1974) fall speed–maximum diameter $(V_t–D_{max})$ formulation for aggregates of unrimed radiating assemblages of plates, side planes, bullets, and columns (Del Genio et al. 2005). After solving for the PSD slope parameter Λ and the critical particle diameters for which the terminal velocity exceeds, is within a small increment of, or is less than the parameterized updraft velocity, simple analytical integration of the mass distribution over the appropriate diameter ranges gives the condensate

fraction that precipitates, is detrained,[1] or is lofted, respectively.

Model E2 GCM configurations (including the CMIP5 versions) that use this partitioning method overproduce detrained cloud ice mass in the upper troposphere by a factor of 2–3 relative to satellite retrieval estimates (e.g., Jiang et al. 2012). One could argue that biases exist in retrieval products, particularly since independent products do not still agree on IWC magnitude (e.g., Wu et al. 2009). However, product dispersion is still much less than this simulation bias. We further suspect that the parameterized updraft velocities in the CMIP5 model are biased high relative to the best observational estimates (Collis et al. 2013). Unrealistically large updraft speeds would also result in too much upper-tropospheric ice, even with realistic PSDs and fall speed formulations (Varble et al. 2011, 2014). However, considering the wealth of new products and in situ datasets available for ice PSDs, and studies revealing that ice PSDs and fall speeds may differ substantially from what we currently assume, we focus here on evaluating and improving the GISS GCM convective ice parameterization [and specifically, we address the less dense ice species treatment, while retaining the PSD and terminal velocity assumptions for dense ice (i.e., graupel) used in Del Genio et al. (2005)]. Section 2 describes the field campaign data, the satellite and reanalysis data used for model comparison, and the GCM configuration used for testing the convective ice parameterization. The new convective ice parameterization is discussed in section 3. Section 4 provides comparisons of the model IWC output to *CloudSat* satellite estimates and additional discussion of other model parameter fields, and future work is discussed in section 5.

2. Data sources and preparation and GCM version

a. Field campaign data sources and IWC computation

We use in situ aircraft data from four field campaigns: the NASA African Monsoon Multidisciplinary Analyses [NAMMA (August–September 2006); Zipser et al. 2009] campaign, the NASA Tropical Composition, Cloud and Climate Coupling [TC4 (July–August 2007); Toon et al. 2010] campaign, the U.S. Department of Energy (DOE) Atmospheric Radiation Measurement

(ARM) Small Particles in Cirrus [SPARTICUS (January–June 2010); Mace et al. 2009; Zhang et al. 2013] campaign, and the DOE ARM–NASA Midlatitude Continental Convective Clouds Experiment [MC3E (April–June 2011); Jensen et al. 2016] campaign.

For NAMMA, data were downloaded from the NASA Global Hydrology Resource Center (http://ghrc.nsstc.nasa.gov). We use the 1-s particle number and projected area distributions [$N(D_{max})$ and $a(D_{max})$, respectively] from the horizontal channel of the 2D stereo probe (2D-S; Lawson et al. 2006) mounted on the NASA DC-8 aircraft. Data collected by the probe can be contaminated by shattered particles, although the algorithm of Lawson (2011) was applied to remove such artifacts. We also use $N(D_{max})$ and $a(D_{max})$ from the Precipitation Imaging Probe (PIP) (courtesy of Andy Heymsfield) in order to quantify PSDs at larger D_{max}. We create composite 2D-S–PIP PSDs following the methodology of Fontaine et al. (2014). The NASA DC-8 Meteorological Measurement System (MMS) instruments (Scott et al. 1990) provide aircraft altitudes, geographic coordinates, pressure, and in situ temperatures. For NASA TC4, data from the DC-8 aircraft were downloaded from https://espoarchive.nasa.gov/archive/browse/tc4. PSD and in situ environmental data are provided from the same instruments as those discussed for NAMMA (removal of shattered artifacts was treated similarly, and composite 2D-S–PIP distributions were also created in the same manner).

For SPARTICUS, data from instruments mounted on the Stratton Park Engineering Company, Inc. (SPEC) Learjet were downloaded from the ARM IOP archive (http://iop.archive.arm.gov). We use the composite particle $N(D_{max})$ and $a(D_{max})$ available from the archive. These composite PSDs were derived through use of ice particle information from the forward scattering spectrometer probe (FSSP), 2D-S, and 2D optical array precipitation probe [2D-P; in later flights the high-volume precipitation spectrometer (HVPS) was used], and in addition to probes having shatter mitigating tips (Korolev et al. 2011, 2013), removal of shattered particles (for both FSSP and 2D-S) from the composite PSDs was performed using an algorithm similar to that described in appendix B of Lawson (2011) (P. Lawson 2016, personal communication). Our analysis of composite PSDs only for $D_{max} > 50\,\mu m$ (discussed in more detail later in the text) also mitigates shattered artifacts from the FSSP instrument. Ancillary data extracted (pressure, altitude, and temperatures) were from the Federal Aviation Administration (FAA)-certified reduced vertical separation minimum (RVSM) aircraft measurement system (with the Rosemount temperature probe being used for in situ temperature).

For MC3E, the University of North Dakota (UND) Cessna Citation II research aircraft instruments [e.g., 2D

---

[1] Detrained condensate goes into an anvil cloud whose cloud ice evolution largely follows the Del Genio et al. (1996) water budget formulation for stratiform or large-scale clouds. The parameterized cloud processes (e.g., autoconversion, accretion, and evaporation) that govern anvil cloud ice conversion to stratiform precipitation are left unchanged in this work, and readers are referred to Del Genio et al. (1996) for formulations and related discussion.

cloud imaging probe (2D-C), HVPS, temperature probe, and static pressure probe] sampled PSDs, IWCs, and ambient temperatures from a large meso-scale convective system (MCS) occurring in a warm, humid environment on 20 May 2011. The 2D-C instrument had shatter mitigating tips, and no shattering removal algorithm was applied to the 2D-C and HVPS data. 2D-C and HVPS composite PSDs were provided courtesy of Greg McFarquhar, and additional details are available in Wu and McFarquhar (2016). We constrained these PSDs further by optimally estimating $N(D_{max})$, $a(D_{max})$, and estimated mass distributions $m(D_{max})$ using Doppler radar spectra within a Bayesian estimation framework.

For all campaign PSDs and in situ environment observations, we do the following: 1) average all data to 10-s intervals; 2) interpolate PSD, temperature, and pressure data to common time bins; 3) set to missing all PSD information in bins centered on a D_{max} below a threshold of 50 μm (to further avoid artificially inflated concentrations at low D_{max} because of instrument shattering); and 4) remove all flight leg samples taken at altitudes of less than 7.5 km (if altitude is not available, then we use a pressure cutoff of 400 hPa). The temporal averaging period should partially depend on the density of the cloud sampled as well as the true airspeed (Hallett 2003). Thus, there is uncertainty in its optimal specification, but we keep it fixed to 10 s in this work, consistent with other studies (e.g., Jackson et al. 2015). Deep convective plumes detrain ice particles that slowly sediment adjacent to deep convective columns and grow through aggregation processes as altitudes decrease (Field and Heymsfield 2003). The microphysical process of aggregation occurs after ice detrainment, and in weak updraft environments adjacent to convective turrets. Since we are designing an improved convective ice parameterization for convective plumes (stronger upward motion), we remove near-to-convection flight legs sampling lower cloud altitudes. It is worthwhile to note that in situ data in these regions may be an important component for convective parameterizations employing a mesoscale/organized stratiform anvil parameterization.

For all campaigns except MC3E, we must estimate the bin-wise $m(D_{max})$ and total IWC [simple integration over $m(D_{max})$]. To do this, we apply the Baker and Lawson (2006) mass–area power law to the particle projected area A computed from the $a(D_{max})$ distributions:

$$m = 0.115A^{1.218}. \tag{1}$$

If the mass computed using this m–A relationship is larger than that of a solid-ice sphere of diameter equal to the particle D_{max} (which is not physically possible), we use the solid-ice sphere mass. Another commonly applied relationship involves a power-law formulation between mass and D_{max} ($m = aD_{max}^{b}$) as in Brown and Francis (1995). Baker and Lawson (2006) noted a substantial reduction in RMS error for bin-wise mass computation when particle area versus maximum dimension is used (i.e., two dimensions constraining the problem versus one), although the best technique is still likely dependent on the conditions under which the measurements were made [e.g., Jackson et al. (2012) found that a habit-dependent m–D_{max} relationship outperformed Baker and Lawson (2006) for measurements made in Arctic stratocumulus clouds].

One advantage of using an m–A relationship includes the avoidance of imposing a fixed particle habit m–D_{max} relationship, which implies that individual particle masses (as a function of D_{max}) are permitted to vary as a function of the environment in our new parameterization (detailed further in section 3a). As discussed above, for MC3E, $m(D_{max})$ is determined from a Doppler spectra retrieval framework. It is important to note that we applied the Baker and Lawson (2006) formulation to the MC3E particle projected areas to assess consistency in the computed mass distributions. We found comparable $m(D_{max})$. Such results also support the use of a mass–area power law.

While we acknowledge that small particles (defined here as those with $D_{max} < 50\,\mu$m) are important, especially for cloud radiative effects, our focus on PSDs for $D_{max} > 50\,\mu$m reflects the measurement uncertainty that exists in concentrations for smaller D_{max} [e.g., out-of-focus particle sizes and small and poorly defined field of depth for small ice particles in optical array probes (e.g., Baumgardner and Korolev 1997)] in addition to the uncertainty that arises from shattering during sample collection (Heymsfield 2007; Jackson et al. 2015, and many references therein). Fortunately, shattering artifacts have been found to contribute less than 20% to the total mass (Jackson and McFarquhar 2014). These instrument issues have motivated others to use a similar D_{max} threshold (e.g., Fontaine et al. 2014), and while this threshold has a large effect on $N(D_{max})$, this threshold has less impact on $m(D_{max})$, and thus our mass partitioning parameterization. This is because most of the IWC is found at $D_{max} > 50\,\mu$m in the PSDs analyzed in this work. Specifically, the chosen threshold results in an average underestimation of total IWC by about 0.002 g m^{-3} (the maximum missed is 0.04 g m^{-3} for IWC < 0.6 g m^{-3} and 0.03 g m^{-3} for IWC > 0.6 g m^{-3}), while only around 6% (~0.4%) of the time greater than 1% (>10%) of the IWC mass resides below the threshold.
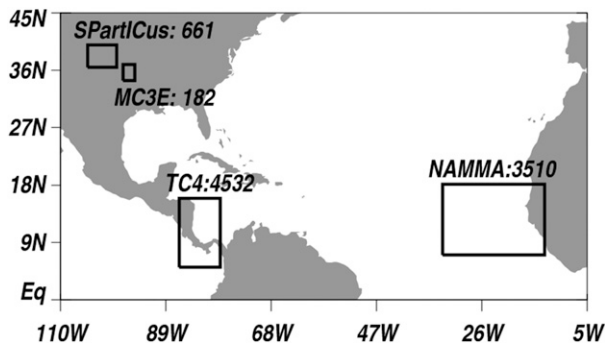
FIG. 1. For each field campaign, the number of 10-s aircraft segments used for in situ PSD analyses. The rectangles outline the geographic domains enclosing the aircraft flight segments.

b. Isolation of convective outflow periods

We must remove aircraft flight legs associated with synoptic cirrus before analysis of the PSDs. Thus, aside from MC3E (for which we only use a 1-h period associated with an MCS), we only retain flight leg segments associated with convection (anvils of varying ages, as well as occasional edges associated with convective turrets) as identified by a listing of "convection sample" dates provided in prior literature. For NAMMA and TC4, key convective periods are discussed in Lawson et al. (2010) and Mitchell et al. (2011). For SPARTICUS, Muhlbauer et al. (2014) and Jackson et al. (2015) provide key dates. Flight leg segments for days not listed as convective in these studies, or those specifically mentioned as synoptic-forcing-driven ice cloud, are removed. What remains after this filtering process is used in the convective ice parameterization development.

The total number of 10-s flight segments extracted from each field campaign is shown in Fig. 1. Three example aircraft flight tracks are shown in Fig. 2; sample segments actually used are drawn in black. As discussed in the introduction, and evident in Fig. 2, the aircraft typically do not fly through the deepest convection (identified by the brightest or reddest colors). Thus, cloud volumes are often sampled from the areas adjacent to the deepest convection; ideally, a sampling of all convective PSDs would serve to inform our convective ice parameterization. Ground-based dual-frequency Doppler radars able to penetrate into deep convective clouds, or research aircraft aiming to sample the highest-water content regions immediately adjacent to deep convection [e.g., High Altitude Ice Crystals/High Ice Water Content (HAIC/HIWC) campaign; Leroy et al. 2015], could inform our convective PSD study at a later date.

c. Datasets for GISS GCM IWC evaluation

We use retrieved cloud ice water and cloud liquid water content (LWC) profiles from the *CloudSat* level-2B

radar-only cloud water content (CWC) product (2B-RO-CWC, version r04; Austin 2007; Austin et al. 2009) for comparison to our IWC simulation. While our focus is on IWC, we evaluate total water content (IWC + LWC) for completeness. We use the orbital-level product (curtain-swath sampling, with a ~2.5-km pixel resolution) files from July 2006 to June 2011. We simultaneously use the *CloudSat* level-2C precipitation product (2C-PRECIP-COLUMN; Haynes et al. 2009, 2013) convective/stratiform flag to first discard all orbital 2B-RO-CWC product pixels that are labeled "convective" and then average all remaining retrievals to a monthly 2.5° × 2.0° resolution (which are the current resolutions of our the GCM output fields). We discard convective pixels for two reasons: 1) the GCM IWC diagnostic represents stratiform IWC, or that which was detrained from the convective plume; and 2) in deeper convection, the *CloudSat* retrieval fails or is degraded more often than in stratiform cloud regimes (partly resulting from substantial rainfall and attenuation). The uncertainty of the *CloudSat* CWC product is typically a factor of 2, mostly due to the PSD assumption used in the retrieval (Jiang et al. 2012).

We use the ECMWF interim reanalysis (ERA-Interim; Dee et al. 2011) 500-hPa vertical velocity fields averaged to the same spatiotemporal resolutions as *CloudSat* (and over the same 5-yr period) to create a composite regime climatology of CWC as a function of a metric related to the dynamical state of the atmosphere. We stratify the CWC climatology as a function of sea surface temperatures (SSTs) as well. The Hadley Centre Sea Ice and Sea Surface Temperature dataset (HadISST, version 1.1) serves as the source for the SST field. This conditional-sampling methodology follows the approach for model evaluation presented in Su et al. (2013).

d. GISS GCM model configuration

We use the GISS Model E2 GCM configuration at a 2.5° × 2.0° horizontal resolution with 40 vertical layers, further described in Schmidt et al. (2014). The Model E2 convective parameterization is described in Kim et al. (2013), with recent developments discussed in Del Genio et al. (2015), but we restate a few important details here. The convective parameterization uses a mass flux approach with the mass flux determined by the vertical mass exchange required for neutral buoyancy at cloud base over an assumed adjustment period (currently 1 h). The total mass flux is divided between two plumes (one weakly entraining, and one more strongly entraining). We use a version of the cold pool I parameterization [described in Del Genio et al. (2015)]. The cold pool parameterization differentiates strong from weak entrainment situations and thus regulates updraft vertical velocity (mostly
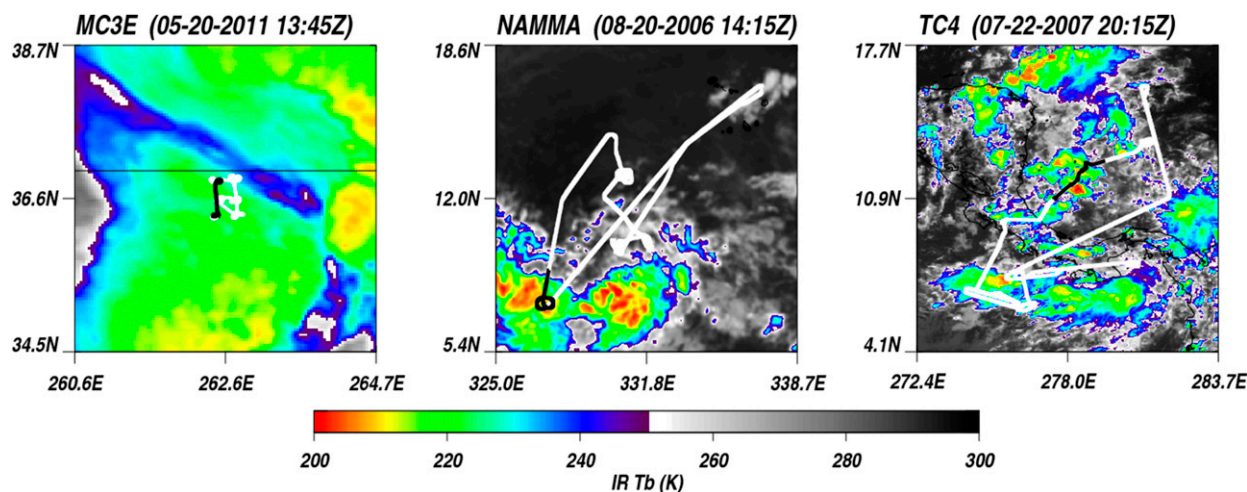
FIG. 2. Sample aircraft flight legs (white lines) superposed on satellite IR brightness temperature images. Example flight leg segments used in this study (adjacent to convection and meeting altitude requirements) are in black.

through regulation of the occurrence of the weakly entraining plume).

Relative to what is documented in Del Genio et al. (2015), the biggest changes to the cold pool I parameterization used in our current GCM setup are as follows: 1) the accumulation of precipitating condensate available for evaporation into the downdrafts begins at the first model level above the initiation of the downdraft instead of beginning at the level for which the downdraft initiates; 2) the PBL pressure depth is used to define the initial pressure depth of the cold pool [instead of a fixed 100-hPa value as discussed for cold pool I in Del Genio et al. (2015)]; 3) the most negatively buoyant mixture fraction for downdrafts is used (instead of a fixed fraction of 0.5); and 4) the entrainment coefficient for the Gregory (2001) entrainment formulation is set to 0.2 (instead of 0.4) for the less-entraining convective plume.

We incorporate the improved convective ice parameterization described in section 3 into the GCM, and integrate the atmosphere-only GCM using prescribed SSTs and sea ice concentrations largely overlapping with the *CloudSat* observing period (5 yr; 2005–09). The HadISST version 1.1 product serves as the source for SST and sea ice lower boundary conditions.

3. Improved convective ice parameterization

In developing new PSD fits and computing ice sedimentation velocities for use in a parameterization, we note the importance of being consistent in our description and use of a particle diameter estimate. Formulas for PSDs and fall speeds are derived according to specific diameter definitions, and the use of inconsistent

diameter definitions can have noticeable impact on computed bulk ice properties as discussed in Wu and McFarquhar (2016). Such errors can also systematically bias parameterizations, as discussed in McFarquhar and Black (2004). Indeed, such an inconsistency was found in our prior treatment of convective ice (where, as it was discussed above, we used the Locatelli and Hobbs (1974) fall speed formulations for unrimed aggregates, but assumed spherical fixed-density ice particles in deriving IWC). Given the impact such inconsistencies may have on the simulated IWC field, in discussing our new parameterization of PSDs and sedimentation velocities, we specifically address our treatment of particle diameter (sometimes in a piecemeal manner, depending on the section) as well as discuss our reasons for converting to a different diameter estimate, if necessary.

a. Particle size distributions for the convective plume

We adopt the normalized particle size distribution approach developed for raindrop size distributions (DSDs) in Testud et al. (2001) and expanded to ice PSDs in Delanoë et al. (2005). The original intention of the normalized size distribution approach was to allow for the raindrop/ice particle diameter and concentration axes to be scaled in such a manner that size distributions become independent of water content and volume-weighted droplet diameters. This technique allows for a convenient presentation of very different PSDs and therefore facilitates better analyses of the "intrinsic shapes" of very different PSDs without the conflating influence of each cloud sample's actual water content and volume-weighted drop diameter.

Unlike what we assumed for ice PSDs in prior versions of the convective ice parameterization (i.e., an
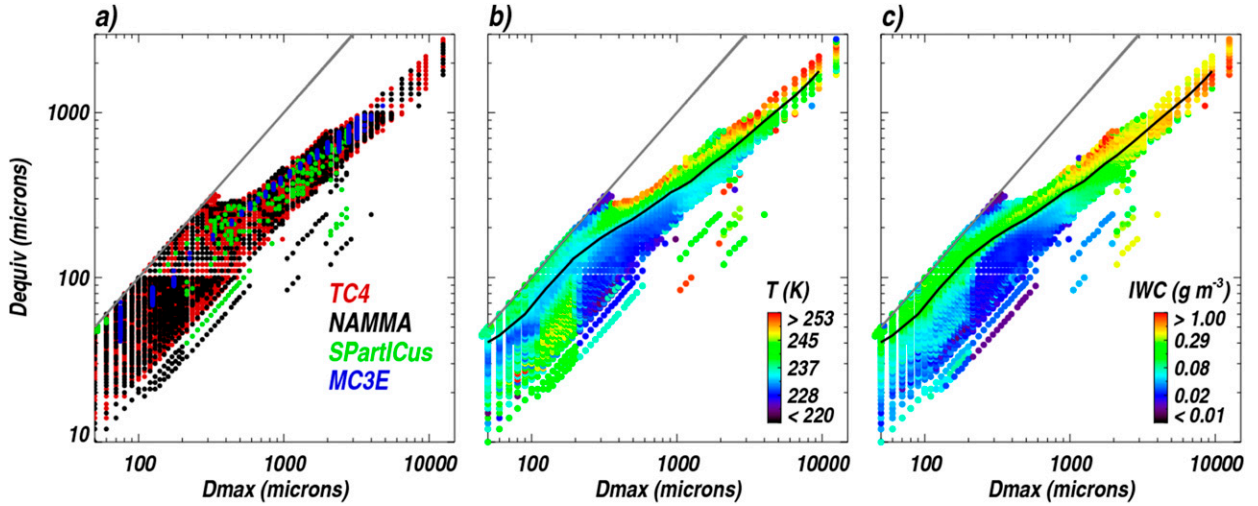
FIG. 3. (a) Scatterplot of the computed D_{eq} as a function of D_{max}, color coded according to the field campaign source. A gray 1:1 line is shown for visual reference. (b) As in (a), except that points are color coded according to the aircraft-sampled in situ temperature. The average D_{eq} as a function of D_{max} is shown by a solid black line. (c) As in (b), except that points are color coded according to the derived in situ total IWC.

exponential distribution), we allow for one more degree of freedom and assume a gamma distribution function for PSDs:

$$N(D_{eq}) = N_0 D_{eq}^{\mu} e^{-\Lambda D_{eq}}, \qquad (2)$$

where D_{eq} is the ice particle equivalent melted diameter. We could have chosen to use D_{max} from the onset in our PSD–gamma formulation, but as will become evident as the equations are laid out, our required analytical computation of PSD moments in the development/use of our parameterization is made much simpler with the use of spherical melted-equivalent particles. Additionally, analytical computation of the third moment (i.e., IWC) of the PSD (quantified as a function of D_{max}) would be in disagreement with the IWC computed from using an m–A relationship (our motivation for using such a relationship was discussed in section 2a), which is not the case if we use melted-equivalent diameters. We can solve for D_{eq} by using the following equation:

$$m(D_{max}) = \frac{\rho_w \pi}{6} D_{eq}^3, \qquad (3)$$

where ρ_w is the density of liquid water ($1000 \, kg \, m^{-3}$).

Of course, PSD information is not reported at a given D_{max} bin center, but is instead provided over a finite bin width. Since we opted to use a m–$a(D_{max})$ formulation and not a m–D_{max} power law for computing $m(D_{max})$, for reasons discussed in section 2a, we are left without a formulation to translate our reported delta D_{max} (δD_{max}, or D_{max} bin widths) to an equivalent delta D_{eq} (δD_{eq}).

So, in practice, for each PSD sample (which has its own unique bin widths, depending on the field campaign), we fit m–D_{max} power laws to each individual computed $m(D_{max})$ in a piecewise fashion using D_{max} ranges of 20–50, 50–100, 100–200, 200–1000, 1000–2000, and >2000 μm, then substitute the m–D_{max} power laws in for $m(D_{max})$ in Eq. (3), and finally solve for δD_{eq} (since we know the actual bin bounds for each campaign reported bin width δD_{max}). In this process, we find that bin widths in D_{eq} space occasionally overlap, and as a result we merge the bins and masses together, carefully ensuring that total IWC is conserved before and after translation to D_{eq}.

Figure 3a shows a comparison of D_{eq} versus D_{max} for all in situ cloud samples used (color coded according to the field campaign to aid in visual inspection). Figures 3b and 3c shade pixel colors according to in situ temperatures and total IWC, respectively. In Fig. 3b, we find that for $D_{max} > 200 \, \mu$m, particles at lower temperatures generally collapse to melted particles with smaller diameters (i.e., ice particles are less dense at lower temperatures). Additionally, in Fig. 3c, we see that larger D_{max} and D_{eq} are associated with larger IWCs in general, while there is clear evidence that for $D_{max} < 2000 \, \mu$m, particles collapse to smaller melted equivalent ones. There are a few anomalies after the conversion to D_{eq}, especially for NAMMA (i.e., smaller D_{eq} for a given D_{max} relative to others). However, these comprise less than 0.5% of the entire database. Noise in the measurements or physics invalidating the mass–area power law in certain environments are also candidates worth exploring for understanding anomalies in the conversion from D_{max} to D_{eq}.

Upon our conversion to D_{eq}, we proceed with normalizing Eq. (2). In the interest of brevity, we simply provide the normalized gamma equation for particle concentration here, but note that details for derivation can be found in Testud et al. (2001) or Delanoë et al. (2005). Proceeding,

$$N(D_{eq}) = N_0^* \frac{\Gamma(4)}{4^4} \frac{(4+\mu)^{(4+\mu)}}{\Gamma(4+\mu)} \frac{D_{eq}^{\mu}}{D_m^{\mu}} e^{-(4+\mu)D_{eq}/D_m}, \quad (4)$$

where

$$N_0^* = \frac{4^4}{\rho_w \pi} \frac{\text{IWC}}{D_m^4} \quad (5)$$

and

$$D_m = \frac{\int N(D_{eq})D_{eq}^4 dD}{\int N(D_{eq})D_{eq}^3 dD}. \quad (6)$$

Substituting Eq. (4) into Eq. (6), followed by integration, allows for the volume-weighted diameter D_m to be simplified and rewritten as $D_m = (\mu + 4)/\Lambda$. Trivially, Eq. (4) can be converted to a particle mass concentration equation given that all particles are now melted liquid water spheres of diameter D_{eq}. Convective plume bulk IWC and temperature are diagnosed in the cumulus parameterization. To parameterize ice mass partitioning in the convective plume, we must seek to relate two free parameters (μ and D_m) to these plume characteristics. In actuality, these two PSD parameters are likely related to a number of environmental descriptors; however, we are limited by what can be gleaned from in situ observations at this point: an estimate of IWC, and ambient temperature. Fortunately, a key parameter of the normalized PSD (D_m) is strongly related to the parameters characterizing the convective plume [the joint correlation of $\ln(D_m)$ with IWC and temperature is >0.8, as discussed below], adding substantial advantage to using PSDs normalized in this manner.

Figures 4a and 4b show the relationship between D_m and temperature and IWC for each field campaign. We can see that as one traverses the range of temperatures and IWCs, particle diameters vary substantially: from 100–150 μm at the lower magnitude end to 300–350 μm at the higher end. In the more familiar D_{max} space, Fig. 3 suggests that this corresponds to an order of magnitude difference in D_{max} (from ~200 μm at the low end to ~1200 μm at the high end).

With IWC available in the convective plume, in addition to needing D_m, knowledge of one additional moment of the PSD will enable an analytical solution to μ. Consider a general expression for the ratio of moments (M_{ij}; ratio of ith moment to jth moment of the PSD, where i and j are both positive integers):

$$M_{ij} \equiv \frac{\int_0^{\infty} N(D_{eq})D_{eq}^i dD_{eq}}{\int_0^{\infty} N(D_{eq})D_{eq}^j dD_{eq}} = \frac{D_m^i}{D_m^j} \frac{\Gamma(\mu+1+i)}{\Gamma(\mu+1+j)} \frac{(\mu+4)^j}{(\mu+4)^i}, \quad (7)$$

where we have arrived at the analytical expression on the far right-hand side after performing a change of variables from D_{eq} to Ψ ($\equiv D_{eq}/D_m$). Of course, D_m is the special case of M_{ij} for $i = 4$ and $j = 3$. We see from Eq. (7) that aside from choosing $M_{ij} = D_m$, we are free to choose another ratio that permits an analytical solution to μ. However, with our eye on parameterization, a physical interpretation to the moment ratio we choose, as well as dependence on temperature and/or IWC, is most appealing (as opposed to a parameter not available from the in situ data, or GCM convective plume). For $\delta = |i - j|$, the simplest expression for μ is achieved when $\delta = 1$, and as δ increases past unity, the solution for μ becomes increasingly difficult to solve analytically. Besides D_m, M_{32} ($\equiv D_a$; the particle area-weighted diameter, analogous to an "effective" diameter) is among the more physically meaningful moment ratios (unlike, for instance, M_{65}, M_{54}, or M_{21}), and so we choose this as our second piece of information needed for determining μ. (It should be noted that while the mean particle diameter M_{10} is a reasonable candidate, we find that the joint correlation of M_{10} with temperature T and IWC is lower relative to other moment ratios). Setting $i = 3$ and $j = 2$, the rhs of Eq. (7) can be rearranged, and we can solve for μ:

$$\mu = (3D_m - 4D_a)/(D_a - D_m). \quad (8)$$

While we constrain the solution to the parameters of the normalized PSD using the M_2, M_3, and M_4 moments, other studies have solved for the parameters of the traditional gamma distribution using different bulk moments [e.g., M_1, M_2, and M_6 computed from analytically integrating the gamma function from 0 to D_{max} in Heymsfield et al. (2002) and McFarquhar et al. (2015)].

For each field campaign, Figs. 4f and 4g show the variation of D_a with temperature and IWC, respectively. The vertical "spikes" of concentrated points in Figs. 4a and 4f are the result of aircraft slicing cloud fields at similar cruising altitudes (and thus, similar temperature levels). Temperature and IWC binned averages of D_m and D_a (averaged without reference to the field campaign
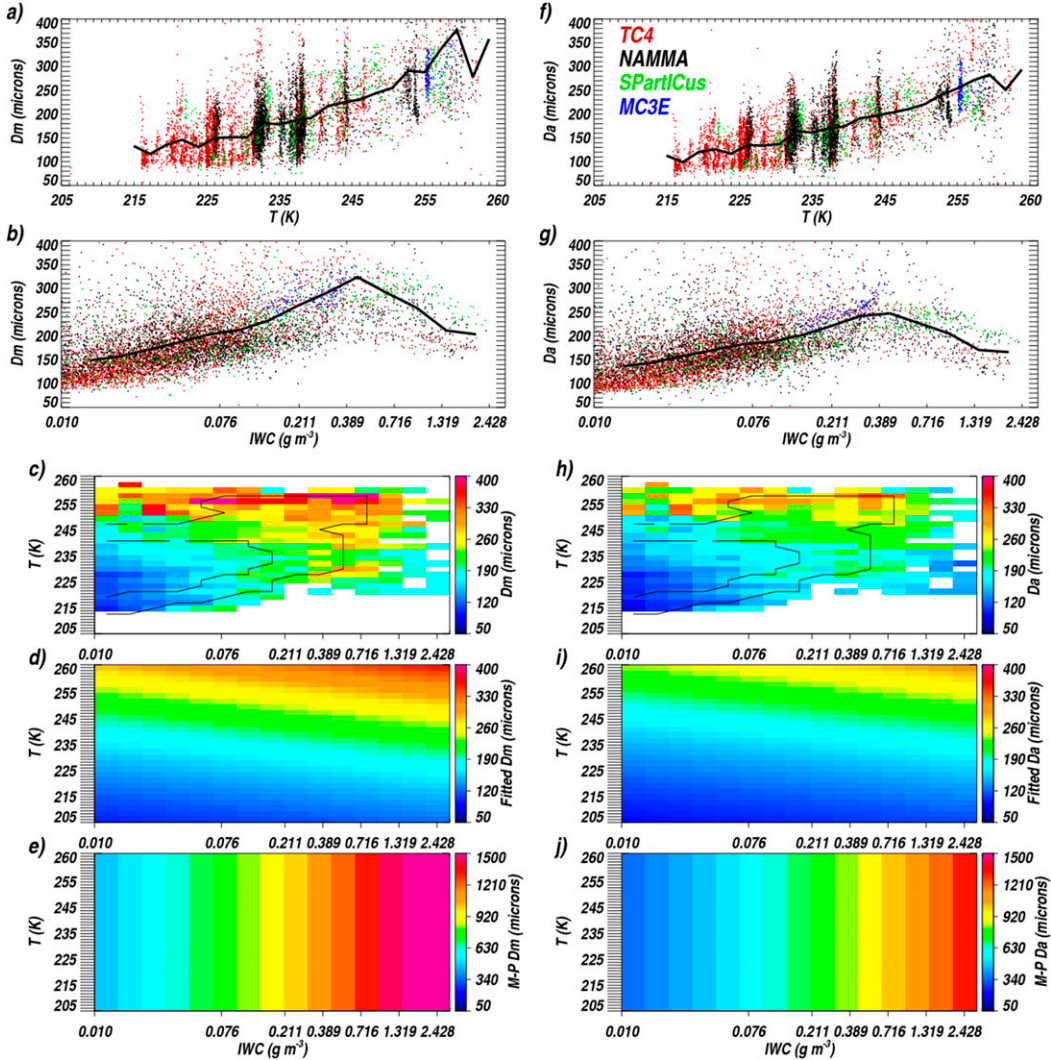
FIG. 4. (a) The mean volume-weighted D_m plotted as a function of in situ T, color coded according to campaign source, with the bin-average D_m (as a function of T) superposed in black; (b) as in (a), but plotted as a function of IWC. (c) An average of all in situ derived D_m plotted as a function of IWC and T, with thin solid black lines denoting sample count thresholds [outer (inner) enclosing line denoting a minimum of 10 (50) samples]; (d) the empirical fit to D_m [shown in (c)] formulated as a function of IWC and T; and (e) D_m as a function of IWC and T, assuming a M-P exponential distribution. Note the change in the magnitude ranges for the M-P PSD fit. (f)–(j) As in (a)–(e), but for the melted-particle cross-sectional D_a.

source) are shown in Figs. 4c and 4h, respectively. After tallying the bin averages, we find that the maximum joint correlation between {temperature, ln(IWC)} and either ln(D_m) or ln(D_a) is approximately 0.85. We therefore parameterize D_m and D_a as a function of temperature and IWC, and arrive at the following relationships:

$$D_m = e^{(C_{m1})} e^{(C_{m2} T)} \text{IWC}^{(C_{m3})} \quad \text{and} \quad (9)$$

$$D_a = e^{(C_{a1})} e^{(C_{a2} T)} \text{IWC}^{(C_{a3})}, \quad (10)$$

where T is in kelvin, IWC is in grams per cubic meter, and D_m and D_a are in meters. The coefficients for Eqs.

(9) and (10) are found in Table 1. The fitted D_m and D_a are shown in Figs. 4d and 4i, respectively. With our parameterized D_m and D_a, and resulting diagnosed μ, we now have everything we need to determine the PSD in our convective ice parameterization.

Given the GISS GCM history of assuming an M-P PSD in its convective ice parameterization, we provide the M-P D_m and D_a in Figs. 4e and 4j. The first key point is that for a given IWC, there is no variation of mean equivalent diameter with temperature, inconsistent with the in situ data. The more striking result is the drastic difference in the particle

TABLE 1. Coefficients for D_m [Eq. (9)] and D_a [Eq. (10)] fits to temperature and IWC.

D_m coefficients			D_a coefficients			V_m coefficients			
C_{m1}	C_{m2}	C_{m3}	C_{a1}	C_{a2}	C_{a3}	V_{m1}	V_{m2}	V_{m3}	V_{m4}
−12.9852	0.019 271 6	0.043 603 0	−12.8023	0.017 867 6	0.040 255 9	−3.137 02	0.022 001	0.083 958 7	−0.245 808

diameter magnitudes between the two PSD assumptions (importantly, note the difference in color bar scales), where overall, except for the highest-temperature and lowest-IWC portion of the state space, the M-P D_m and D_a are several factors larger than the mean diameters we compute using the field campaign data. This result conflicts with an original motivation for reevaluating the convective ice parameterization in the GCM: the high IWC bias relative to observations. All other parameters being equal (including no change in the treatment of graupel), these new findings suggest that, overall, particles are much smaller, and therefore detrained ice and high cloud would be expected to increase upon using the new parameterized gamma PSD. However, as will be discussed later, new terminal fall velocity formulations counteract this and result in greater particle fall speeds.

The computed N_0^* and μ parameters, spanning a wide range of temperatures and IWCs, are shown in Fig. 5. Because particle diameters were converted to melted-equivalent diameters, these parameters [including N_0 from Eq. (2)] are not directly comparable to the more "traditional" gamma distribution parameters shown for $D_{\max}$ distributions. The following steps facilitate a fair comparison, although we emphasize that the equations derived in the remainder of this section (section 3a only) are not used in the convective ice parameterization. In $D_{\max}$ space, let the particle number concentration from $D_{\max}$ to $D_{\max} + \delta D_{\max}$ be written (assuming a generalized gamma form):

$$N(D_{\max}: D_{\max} + \mathrm{d}D_{\max}) = N_{0_2} D_{\max}^{\mu_2} e^{-\Lambda_2 (D_{\max}) k_2} \, \mathrm{d}D_{\max},$$
(11)

where the "2" subscript is appended to each of the parameters to ensure no confusion between the equivalent gamma parameters presented for PSDs in D_{eq} space [Eq. (2)]. If we let $D_{\mathrm{eq}} = a(D_{\max})^b$, from which $\delta D_{\mathrm{eq}} = ab(D_{\max})^{b-1}\delta D_{\max}$ follows, then after rearranging and solving for $D_{\max}$, and substituting both into the rhs of Eq. (11) [in order to develop an equivalent $N(D_{\mathrm{eq}})$ equation], we arrive at the following useful expressions that allow for quick translation of gamma parameters in $D_{\max}$ space to those in D_{eq} space, as denoted in Eq. (2):

$$N_0 = N_{0_2}/[ba^{(\mu_2+1)/b}],$$
(12)

$$\mu = (\mu_2 + 1)/b, \quad \text{and}$$
(13)

$$\Lambda = \Lambda_2 a^{-k_2/b}.$$
(14)

We find that $a = 0.06 \, \mathrm{m}^{1-b}$ and $b = 0.73$ yields the maximum correlation with the in situ derived points in Fig. 3a. For the prior GISS convective cloud ice formulation, $D_{\max}$ represented spherical ice particles of density
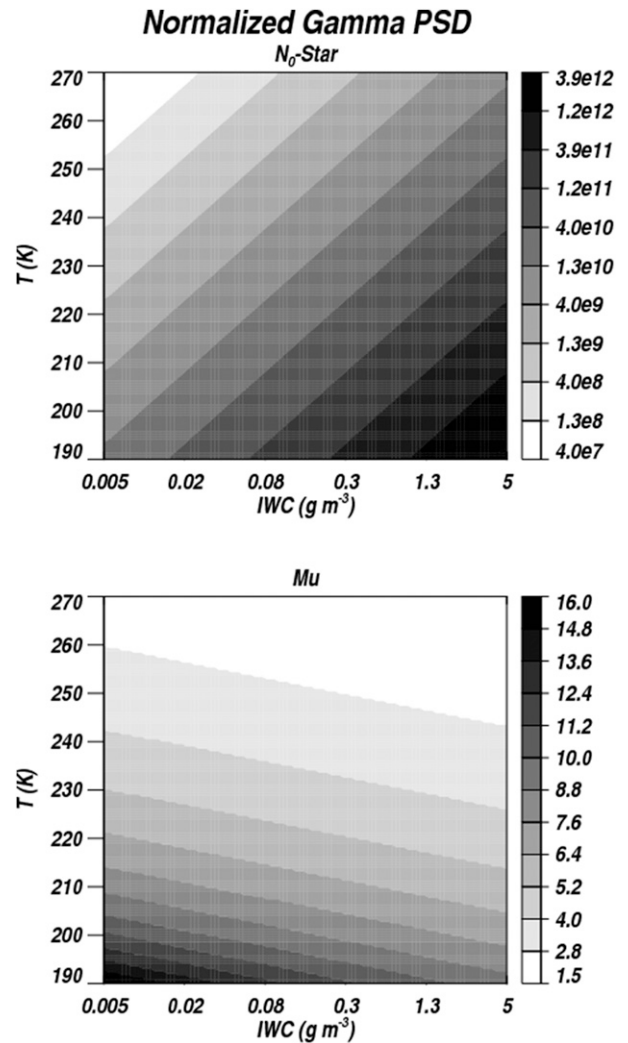

FIG. 5. For the normalized gamma distribution, (top) the intercept parameter N_0^* and (bottom) μ parameter as a function of IWC and T.

approximately $100\,\mathrm{kg\,m^{-3}}$. That assumption leads to $a = 0.464\,\mathrm{m^{1-b}}$ and $b = 1$ (derived analytically). With this information, we can now understand why the M-P D_m and D_a magnitudes are so large, given that exponential distributions are sometimes thought of as comprising a substantial number of small particles. From Eqs. (12) and (13), our M-P intercept and dispersion parameters ($8 \times 10^6\,\mathrm{m^{-4}}$ and 0) convert to approximately $1.7 \times 10^7\,\mathrm{m^{-4}}$ and 1, respectively, when our prior assumptions from Del Genio et al. (2005) are used (i.e., for spherical particles, $a = 0.464\,\mathrm{m^{1-b}}$ and $b = 1$). Figure 5 shows that μ is a factor of 1–15 higher, and since $D_m = (\mu + 4)/\Lambda$, we should expect an increase in D_m. However, we find that Λ computed here increases by a factor of 20–100, which overcompensates and leads to a large decrease in D_m. Thus, the significantly increased slope parameter is the reason for the small D_m and D_a we find in Fig. 4. These results are consistent with the discussion of gamma PSD parameter impacts on particle-size weighting in Jackson et al. (2015).

At first glance of Fig. 5, the magnitudes of the normalized gamma PSD μ parameters seem conspicuously large. With $b = 0.73$, Eq. (13) reveals that the conversion from D_{max} to D_{eq} has the interesting effect of significantly increasing μ relative to what we would expect for an identical PSD analysis performed in D_{max} space [where, instead of $\mu \approx 15$ at the lowest T and lowest IWC, with $b \approx 0.7$, our value for μ would collapse to ~ 9.5 in Eq. (13)]. Considering our entire field campaign dataset, we find a median μ of approximately 5, which collapses to the more familiar $\mu \approx 2\text{–}3$ magnitude range (Heymsfield et al. 2013; McFarquhar et al. 2015) when analyzing in D_{max} space.

Using our new parameterization for determining ice particle PSDs, resulting fits superposed on in situ derived PSDs (for widely varying IWC and temperature bins) are shown in Fig. 6. The prior assumed M-P PSDs are also shown. One can see that the new parameterized PSDs nicely reproduce the example in situ derived PSDs in different environments, with substantial improvement relative to the prior fits. However, the new fits do underestimate the number concentrations in these higher IWC scenes for larger D_{eq} (two middle panels in the left column of Fig. 6). The derived mass distributions are shown in the right column of Fig. 6, with axes chosen to ensure that PSDs are visually integrable, permitting easy inspection of where ice mass is concentrated. One can see that despite the underestimation of number concentrations at larger D_{eq}, the fraction of ice mass underquantified with the new fits is minimal.

b. Fall speed formulations for convectively generated ice particles

Prior to now, Locatelli and Hobbs (1974, hereafter LH74) served as the source for particle fall speed

approximations, as discussed in section 1. The particular V_t–D_{max} formulation used in the most recent GISS GCM iteration is provided in Del Genio et al. (2005), and is discussed in our introduction. More recent field campaigns have shed additional light on fall speed assumptions, and considerable differences in fall speeds relative to older formulations have been found. For instance, Heymsfield et al. (2013, hereafter H2013) found that overall (albeit with some diameter dependency), convectively generated ice particle velocities exceed the LH74 estimate by a factor of 2–3. To be clear, the LH74 formulation that was serving as a comparison benchmark is different from the one we utilized in the GCM convection routine (see H2013 for details); however, such large differences at least motivate our reevaluation of the fall speed approximations.

Similar in spirit to this work, which entails synthesizing diverse PSD datasets from various convection regimes, H2013 combined different datasets to develop separate stratiform- and convection-generated particle fall speed formulas as a function of D_{max} and pressure. There is appeal in having just one option for fall speed in that the arbitrariness of imposing the most "correct" fall speed formula among a myriad of options, as was the case when using LH74 formulas, is avoided. Equations (12a)–(12d) from H2013 are adopted here; an equation for pressure correction, which is also D_{max} dependent, is also incorporated. Formulas applicable to particles of diameter D_{max} are not portable to our particles of diameter D_{eq}. Therefore, before our conversion of PSDs to equivalent distributions in D_{eq} space, we apply the H2013 formulas to our original D_{max} distributions, compute a mass-weighted fall velocity for each in situ sample over a range of pressures (1000–100 hPa), and, consistent with the parameterization approach for D_m and D_a, regress the sedimentation velocity on temperature, IWC, and pressure, assuming the following functional form:

$$V_m = e^{(V_{\mathrm{m1}})}e^{(V_{\mathrm{m2}}T)}\mathrm{IWC}^{(V_{\mathrm{m3}})}p^{(V_{\mathrm{m4}})}, \qquad (15)$$

where T is in kelvin, IWC is in grams per cubic meter, pressure p is in hectopascal, and V_m is in meters per second. The coefficients for Eq. (15) are found in Table 1.

The conversion to D_{eq} does not change the sedimentation velocity, so we equate Eq. (15) to a sedimentation velocity in D_{eq} space:

$$V_m(T, \mathrm{IWC}, p) \equiv \frac{\int_0^\infty V(D_{\mathrm{eq}})N(D_{\mathrm{eq}})D_{\mathrm{eq}}^3\,dD_{\mathrm{eq}}}{\int_0^\infty N(D_{\mathrm{eq}})D_{\mathrm{eq}}^3\,dD_{\mathrm{eq}}}, \quad (16)$$
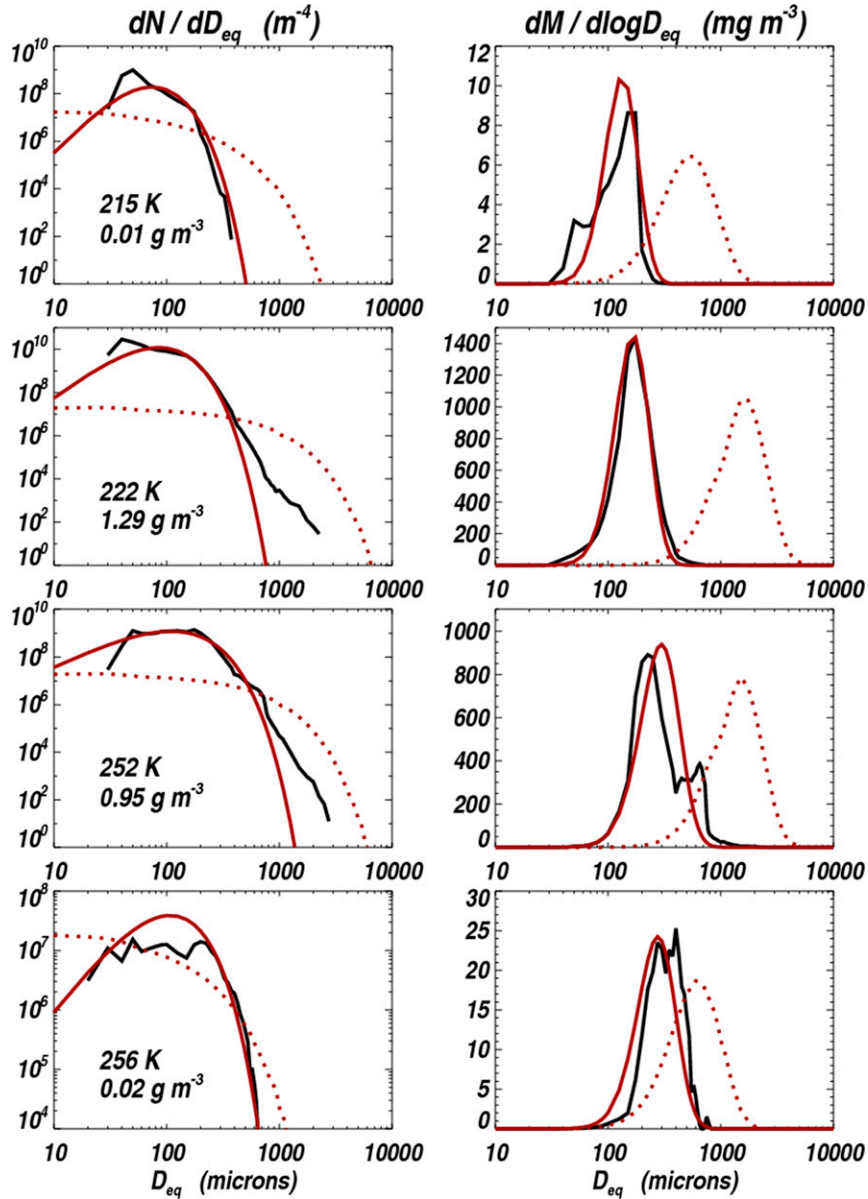
FIG. 6. Field campaign (left) particle number and (right) derived mass concentrations as a function of melted equivalent diameter (solid black) for four different in situ temperature–IWC bins, (top)–(bottom) the total number of samples going into each T–IWC bin: 7, 21, 18, and 6. The corresponding fits to the distributions, derived through use of the IWC–T parameterized D_m and D_a formulations to solve for the normalized gamma distribution parameters, are shown in solid red. The prior assumed GISS GCM M-P exponential PSDs (converted to functions of melted equivalent diameter) are also shown for comparison (dotted red).

where $N(D_{eq})$ is provided by the PSD parameterization developed in section 3a. Our only remaining unknown is $V(D_{eq})$, and so by substituting a power-law formulation $[V(D_{eq}) = \alpha D_{eq}^B]$ for $V(D_{eq})$, and mimicking the approach outlined for manipulating Eq. (7), we arrive at the following expression for V_m:

$$V_m(T, \text{IWC}, p) = \frac{\alpha \Gamma(\mu + 4 + B) D_m^B}{\Gamma(\mu + 4)(\mu + 4)^B}. \quad (17)$$

At this point, we utilize one boundary condition that facilitates "closure" determination of α and B: the fall velocity of small particles. Rearranging our terminal velocity power law, let $\alpha = V(D_{eq\_MIN}) D_{eq\_MIN}^{-B}$, and

substitute for α on the rhs of Eq. (17). While in theory one could choose to use a fall velocity of any sized particle, at small D_{max}, the departure from sphericity is less of an issue, the pressure correction is less of a factor and potentially less prone to bias (H2013), and, because the variation in D_{eq} is smaller (Fig. 3a), we expect that variations in fall velocities are smaller than at larger D_{max}. From H2013 [their Eq. (12b)], at 1000 hPa, particles with $D_{max} \approx 100\,\mu m$ fall at a velocity of approximately $0.16\,m\,s^{-1}$. We also find that a particle at $D_{max} \approx 100\,\mu m$ collapses to a droplet of $D_{eq} \approx 70\,\mu m$ (which becomes our D_{eq_MIN}). Using these values to anchor the fall velocity at the low D_{eq} end, then provided with $V_m(T, IWC, p)$, we can solve for B (which we do iteratively by starting at $B = 0$, and incrementally increasing it until the right-hand side is equivalent to the diagnosed V_m). This method conveniently allows for the V_t–D_{eq} power-law formulation to vary as a function of temperature, IWC, and pressure (for each GCM grid box and time step), which is more physically reasonable since melted particles at a given D_{eq} were originally ice particles at varying D_{max} that fell according to their own geometries and densities.

A comparison of sedimentation velocities for varying PSD and particle terminal velocity assumptions is shown in Fig. 7. The LH74 terminal velocity formulation applied to our prior assumed M-P PSD [i.e. the assumptions in Del Genio et al. (2005) and Kim et al. (2013)] yields the sedimentation velocities shown in Fig. 7a. With our new parameterized PSDs, applying the same LH74 terminal velocity formulations leads to substantially decreased sedimentation velocities (Fig. 7b), consistent with the argument in the prior section that, with the new PSDs, use of the same terminal velocity formulations should lead to decreased sedimentation and even more ice aloft (since mean particle diameters are now much smaller). The new formulations incorporating H2013 formulas, applied to our new PSDs, yield the fall velocities shown in Fig. 7c.

In summary, our new PSD parameterization leads to decreased particle sizes, and thus increased detrainment of ice. However, this is counteracted by new terminal velocity formulations that result in larger sedimentation rates when superposed with the new PSDs (viz., in the regimes where most of the deep convective IWC is found at temperatures higher than 225 K). At this point, we proceed with partitioning [as discussed in the introduction, and as outlined for the M-P PSD in Del Genio et al. (2005)]: we find the critical D_{eq} for which the terminal velocity exceeds the parameterized updraft velocity, and by performing analytical integration of the mass PSD over the appropriate diameter ranges, we arrive at the ice condensate fraction that precipitates.
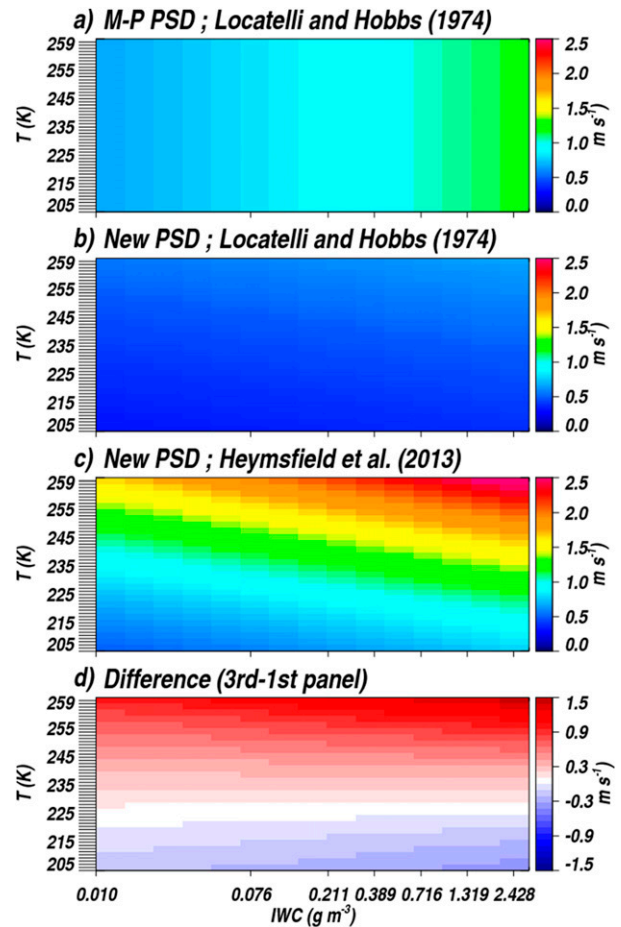

FIG. 7. As a function of IWC and T at a reference pressure of 1000 hPa, (a) the mass-weighted terminal fall velocity using a M-P exponential PSD and LH74 $V(D_{max})$ formulation for aggregates of unrimed radiating assemblages of plates, side planes, bullets, and columns; (b) same $V(D_{max})$ relationship, but applied to new parameterized PSDs; (c) using the H2013 $V(D_{max})$ formulation for convective-outflow ice applied to the new parameterized PSDs; and (d) the mass-weighted terminal fall difference as a function of IWC and T [new PSD (H2013) minus M-P exponential PSD (LH74)].

When the terminal velocity at D_{eq} is within a small increment of the updraft velocity, ice condensate is detrained. For the terminal velocity at D_{eq} less than the updraft velocity, ice is lofted.

4. GCM simulations with improved convective ice parameterization

GISS Model E2 simulated global-average IWP has been steadily decreasing since phase 3 of the Coupled Model Intercomparison Project (CMIP3). Specifically, Jiang et al. (2012) showed an IWP decrease of about $130\,g\,m^{-2}$ from CMIP3 to CMIP5 (the global mean was

$\sim$230 g m^{-2} for CMIP3 and $\sim$100 g m^{-2} in CMIP5). The post-CMIP5 configuration (atmosphere-only run) of the GCM, which included changes to planetary boundary layer (PBL) turbulence and the moist convective parameterization as described in Stanfield et al. (2014), slightly increased IWP relative to that simulated in CMIP5 (global mean of $\sim$105 g m^{-2}). Progressing further, the cold pool parameterization of Del Genio et al. (2015), which is an important component of our control GCM, resulted in another large reduction in the IWP climatology relative to prior GCM configurations. The cold pool parameterization serves to regulate the less entraining (i.e., deep convective) plume. Because this convective plume is responsible for most of the IWC lofted in deep convective regions, a cap on its occurrence directly implies that less IWC will be detrained in the upper troposphere. The IWP climatology for this control GCM is shown in Fig. 8a. Consistent with the physical argument presented, the global mean IWP decreased to about 70 g m^{-2}.

With the improved convective ice parameterization incorporated into the GCM, the global mean IWP decreases further to about 54 g m^{-2} (Fig. 8b). This global decrease is largely driven by deep convective regime decreases in IWP over the intertropical convergence zone (ITCZ), the South Pacific convergence zone (SPCZ), the western Pacific warm pool (WPAC), monsoon regions of the northern Indian Ocean, and most of the Caribbean Sea. In WPAC, for instance, decreases in IWP are on the order of 100–200 g m^{-2}; this represents an approximate 30%–50% decrease in IWP for many regions. For most regions, the decreases bring the climatology into closer agreement with *CloudSat* estimates (e.g., monsoon regions, WPAC, SPCZ, and Caribbean Sea). Discrepancies increased, however, over the eastern Pacific portion of the ITCZ, as well as over some continental regions (e.g., portions of the United States and South America).

At first glance, the slight increase in IWP over the highest latitudes seems surprising since our parameterization changes are all related to the convection scheme; however, our GCM retuning process required to bring the atmospheric model back into global radiative balance [see discussion in Mauritsen et al. (2012)] is responsible for these systematic increases. We find that this tuning process has little impact on the IWC in the deep convective regions. For this GCM version, in order to tune, we found the ideal combination of relative humidity thresholds for cloud formation, autoconversion factors governing stratiform ice and liquid precipitation onset, and stratiform liquid/ice cloud effective radii [some of these are discussed in Schmidt et al. (2014)]. Here, the "ideal" combination of parameters is the one that leads
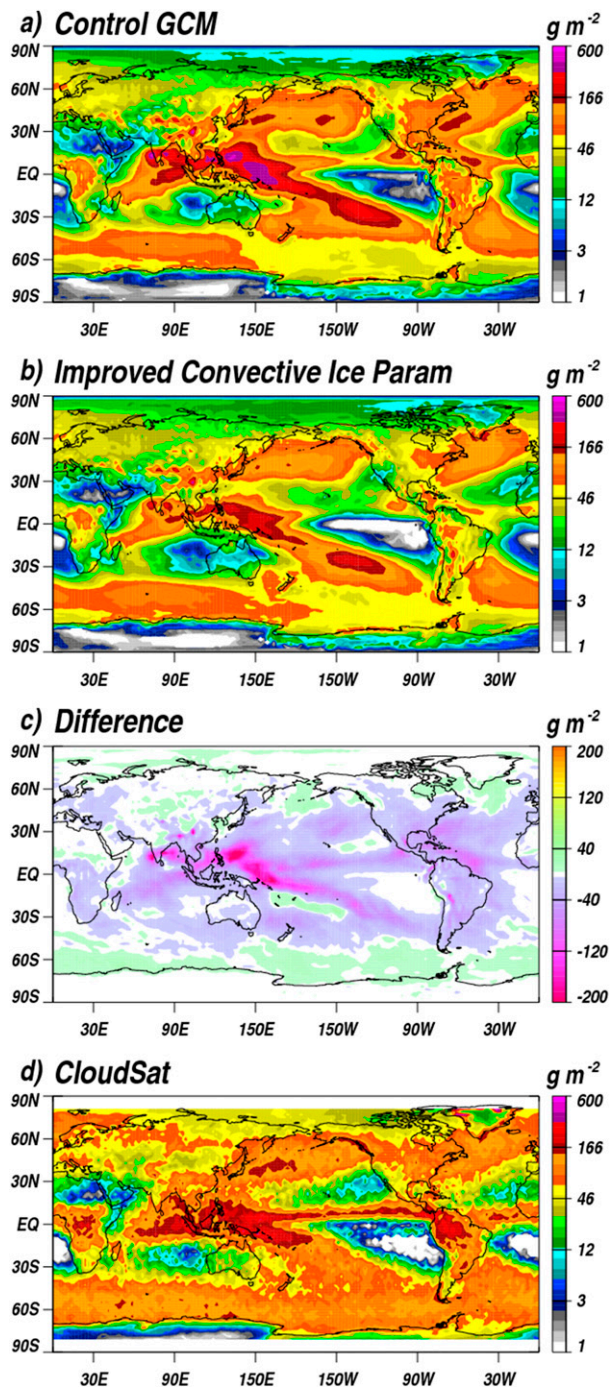

FIG. 8. (a) The IWP climatology from the GCM configured with a version of cold pool I parameterization (Del Genio et al. 2015), (b) the IWP climatology with the improved convective ice parameterization, (c) the difference between the two GCM configurations, and (d) *CloudSat* IWP climatology.

to global radiative balance coincident with minimized regional discrepancies in radiation fields, water vapor fields, and cloud fields based on climatological comparisons to a number of observational datasets.
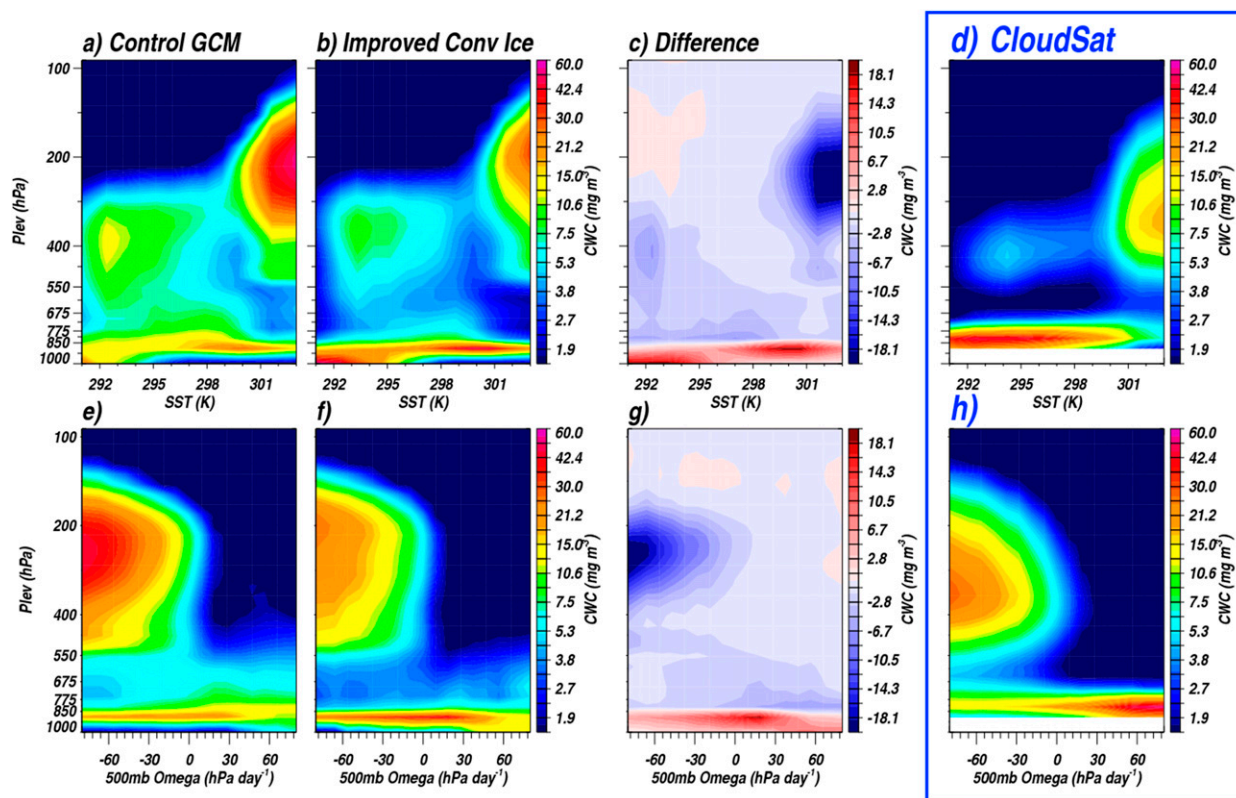
FIG. 9. (a) The CWC climatology conditioned on SST for the GCM configured with a version of cold pool I parameterization (Del Genio et al. 2015), (b) the CWC with the improved convective ice parameterization (improved PSDs and fall speed formulations), (c) the difference between the two GCM configurations, and (d) *CloudSat* CWC climatology. (e)–(h) As in (a)–(d), but computed as a function of ERA-Interim 500-hPa vertical velocity.

Figure 9 is more revealing for determining which environmental states are associated with the greatest decreases in IWC. Not surprisingly, the deep convective regions—associated with higher SSTs, and upward mid-tropospheric vertical velocity—are characterized by the most substantial decreases in IWC. The sedimentation of ice condensate in the deep convective plume is drastically increased at higher temperatures (Fig. 7c); thus, we would expect the biggest decreases in IWC at altitudes immediately above the freezing level. However, at these levels in the convective plume, a substantial fraction of ice is partitioned into the graupel category, as described in Kim et al. (2013), and since no changes to the dense ice assumptions were made, the greatest decreases in IWC are realized at higher altitudes from 350 to 175 hPa (where T ranges from ~255 to 210 K). At the lower T end of this spectrum, particles fall more slowly than they previously did (Fig. 7d). However, by this time, newly formed condensate is unable to replenish the amount that would have been lofted, but was instead precipitated below. Thus, simulated IWC is still significantly decreased at these higher altitudes. For the most part, increases in

liquid water content (e.g., below 775 hPa) and much smaller decreases in IWC (over lower SSTs) are not the result of our new parameterization. These changes, are again, driven by the model retuning process.

Quantification of the specific regional and global *CloudSat* and GCM biases are not presented here given that there are reasons to expect legitimate biases. For one, radar returns, even from large precipitating ice particles, are used to retrieve IWC; thus, IWC from the *CloudSat* product is best considered a total (cloud plus precipitation) IWC product (Waliser et al. 2009), while in Model E2, IWC is a "cloud only" condensate diagnostic. Second, the PSD and ice densities assumed in the CWC retrieval have a large impact on the IWC retrieved (Woods et al. 2008). Such retrieval peculiarities suggest that care must be taken when quantifying satellite–GCM differences, and to this end, we use *CloudSat* IWC as a "best" qualitative estimate, but reserve discussion of specific magnitude biases for the time when such issues can be better tackled.

Before tuning the GCM, it is important to understand what impact the improved physics has on water vapor,

rainfall, and radiation fields. Relative to the control GCM, globally, we find little change in composite-average total precipitable water (TPW), and gridbox changes are seemingly uncorrelated with IWP changes (Fig. 10a). We find similar results for water vapor at all model altitudes. Perhaps the biggest change is in precipitation. Since we are precipitating more condensate, there is an unsurprising increase in global convective rainfall (1.21–1.36 mm day^{-1}) and a slightly over-compensating decrease in global stratiform rainfall (1.72–1.53 mm day^{-1}). The autoconversion to stratiform precipitation increases as IWC increases (Del Genio et al. 1996), which explains why the decrease in stratiform precipitation is very correlated with stratiform IWC or IWP changes (Fig. 10c). For the 20°S–20°N geographic domain, the percent of rainfall classified as stratiform drops from 45% to 35%. Schumacher and Houze (2003), over this same domain, derived an estimate of 40% from TRMM Precipitation Radar (PR) retrievals. However, TRMM PR misses a substantial amount of lighter, shallower rain (e.g., Berg et al. 2010) that may be produced by shallower convection. If that is the case, the estimate of 40% could be high.

Outgoing longwave radiation (OLR) and absorbed shortwave (SW) radiation changes were less correlated with the change in IWP than was anticipated (for both radiation components, the correlation with the change in IWP is less than 0.3). Whether or not this is realistic with our current GCM configuration has to be determined. On one hand, the cloud fields most affected by the ice parameterization were already very optically thick; therefore, despite decreasing IWC substantially, the deep convective cloud itself is still geometrically, and optically, thick. As a result, reflected SW may change minimally. On the other hand, the smaller composite-average change in SW may have to do with our treatment of the ice cloud effective radius. By decreasing IWC or high cloudiness, we decrease albedo, and in turn more SW radiation is absorbed. However, in the current stratiform cloud routine, the same number concentration is always assumed, regardless of the IWC magnitude. Therefore, when IWC decreases substantially, particle radius decreases in tandem. Smaller particles are more reflective, which increases the albedo, and thus partly counteracts the decreased albedo that would have occurred with decreasing IWC. The physical realism of this latter possibility will have to be investigated in future GCM versions.

5. Conclusions

We have developed an improved parameterization of the size distribution and terminal velocities of ice
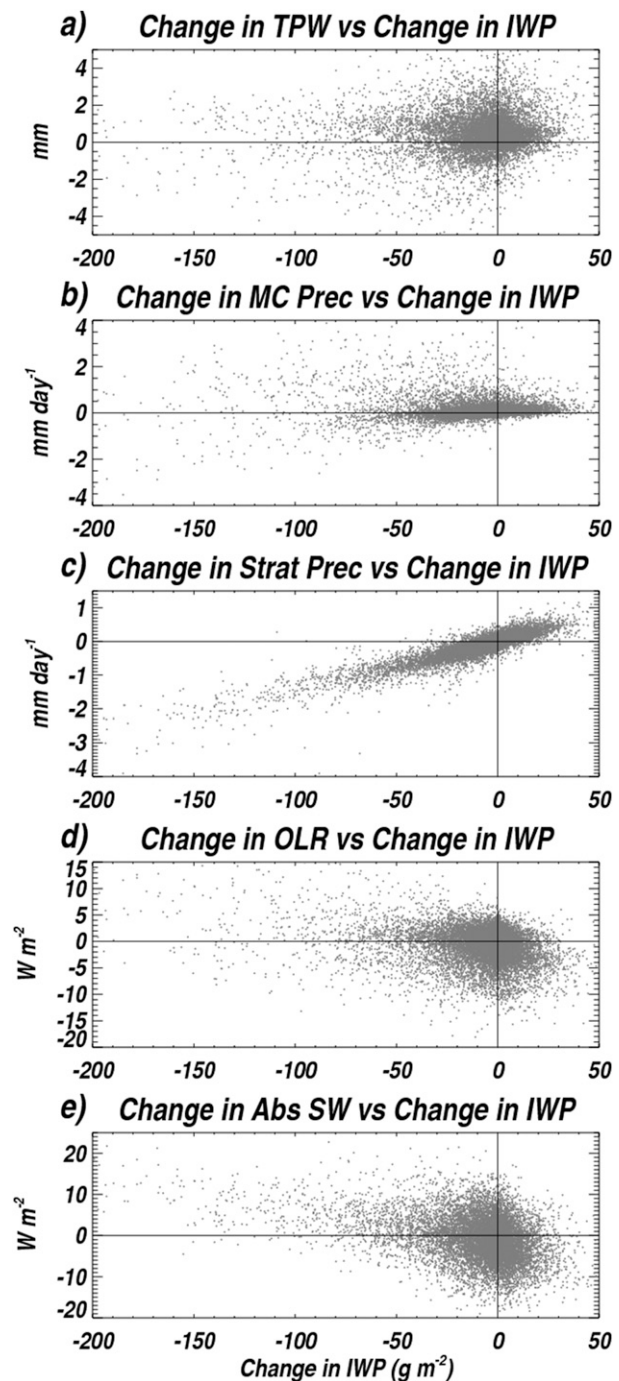
FIG. 10. (a) The change in TPW as a function of the change in IWP. The change refers to TPW and IWP in the GCM with the improved convective ice parameterization minus the TPW and IWP in the GCM configured with a version of the cold pool I parameterization (Del Genio et al. 2015); (b) as in (a), but for moist convective precipitation rate vs IWP; (c) as in (a), but for the stratiform precipitation rate vs IWP; (d) as in (a), but for OLR vs IWP; and (e) as in (a), but for absorbed SW radiation vs IWP.

particles in a convective updraft. The PSD parameterization is based on in situ aircraft observations made in close proximity to deep convection during a number of NASA and DOE field campaigns. In accordance with the relationships derived from the in situ data, the PSD parameters now explicitly vary with temperatures and IWC. For particle terminal velocities, we now rely on H2013. Their approach is similar to ours in that multiple field campaigns inform the development of generalized convective–ice fall speed formulations. The improved parameterization leads to smaller mass-weighted-diameter ice particles in the convective updraft relative to the prior GCM parameterization. However, these smaller particles fall more quickly with the new terminal velocity formulations. When combined with the GCM's parameterized convective updraft velocity, the net effect is to increase sedimentation of convective ice generated in the convective updraft, which in turn leads to decreased IWC in deep convective regions. Because our ice PSDs and terminal velocities are representative of regions adjacent to deep convective turrets, future improvements to the parameterization should include a better representation of dense ice or graupel PSDs and fall velocities characteristic of convective updraft cores. Ground-based multiple-frequency Doppler radar analyses of deep convection columns, or field campaigns such as HAIC/HIWC, during which aircraft sampled regions of deep convection, higher IWC, and denser ice, may prove useful in such an endeavor.

Our focus in this study was on using observations to facilitate a more realistic partitioning of ice mass in convective plumes. Revisiting our formulations for this process was in part motivated by the high IWP bias that has existed in many prior configurations of the NASA GISS GCM. However, the evolution of organized convection, and in particular, stratiform anvil clouds, is greatly impacted by the treatment of detrained ice. The cold pool parameterization of Del Genio et al. (2015) served as a first step toward preparing the GCM for organized convection simulation. In this work, because PSDs, temperatures, and IWCs were derived from portions of cloud systems straddling the deep convective tower and associated anvil, we expect that the parameterization developed here will serve as a starting point for simulating stratiform anvil cloud, the successful simulation of which requires information on the coupling between temperatures, detrained condensate, PSDs, fall speeds, and radiation for these cloud types. Thus, this convective ice parameterization serves as another step toward aggregating the physics components needed for organized convection simulation.

Finally, we note that there is little consensus on whether clouds associated with deep convection matter for climate sensitivity beyond their change in altitude in a warming climate (Boucher et al. 2013). The parameterization presented here regulates detrainment as a function of ice cloud properties that, along with the convective dynamics, should respond in a physically plausible way to a climate change. It therefore represents a first step toward the goal of eventually constraining the deep convective contribution to cloud feedback.

REFERENCES

Austin, R., 2007: Level 2B Radar-only Cloud Water Content (2B-CWC-RO) Process Description Document, version 5.1. *CloudSat* Data Processing Center, 24 pp. [Available online at ftp://ftp.cira.colostate.edu/ftp/CloudSat/Docs/2B-CWC-RO_PDICD.P_R04.20071021.pdf.]

——, A. J. Heymsfield, and G. L. Stephens, 2009: Retrieval of ice cloud microphysical parameters using the *CloudSat* millimeter-wave radar and temperature. *J. Geophys. Res.*, **114**, D00A23, doi:10.1029/2008JD010049.

Baker, B., and R. P. Lawson, 2006: Improvement in determination of ice water content from two-dimensional particle imagery. Part I: Image-to-mass relationships. *J. Appl. Meteor. Climatol.*, **45**, 1282–1290, doi:10.1175/JAM2398.1.

Baumgardner, D., and A. Korolev, 1997: Airspeed corrections for optical array probe sample volumes. *J. Atmos. Oceanic Technol.*, **14**, 1224–1229, doi:10.1175/1520-0426(1997)014<1224:ACFOAP>2.0.CO;2.

Berg, W., T. L'Ecuyer, and J. M. Haynes, 2010: The distribution of rainfall over oceans from spaceborne radars. *J. Appl. Meteor. Climatol.*, **49**, 535–543, doi:10.1175/2009JAMC2330.1.

Bony, S., and Coauthors, 2006: How well do we understand and evaluate climate change feedback processes? *J. Climate*, **19**, 3445–3482, doi:10.1175/JCLI3819.1.

——, and Coauthors, 2015: Clouds, circulation, and climate sensitivity. *Nat. Geosci.*, **8**, 261–268, doi:10.1038/ngeo2398.

Boucher, O., and Coauthors, 2013: Clouds and aerosols. *Climate Change 2013: The Physical Science Basis*, T. F. Stocker et al., Eds., Cambridge University Press, 571–658, doi:10.1017/CBO9781107415324.016.

Brown, P. R. A., and P. N. Francis, 1995: Improved measurements of the ice water content in cirrus using a total-water probe. *J. Atmos. Oceanic Technol.*, **12**, 410–414, doi:10.1175/1520-0426(1995)012<0410:IMOTIW>2.0.CO;2.

Clement, A. C., and B. J. Soden, 2005: The sensitivity of the tropical-mean radiation budget. *J. Climate*, **18**, 3189–3203, doi:10.1175/JCLI3456.1.

Collis, S., A. Protat, P. T. May, and C. Williams, 2013: Statistics of storm updraft velocities from TWPICE including verification with profiling measurements. *J. Appl. Meteor. Climatol.*, **52**, 1909–1922, doi:10.1175/JAMC-D-12-0230.1.

Comstock, J. M., and Coauthors, 2007: An intercomparison of microphysical retrieval algorithms for upper-tropospheric ice clouds. *Bull. Amer. Meteor. Soc.*, **88**, 191–204, doi:10.1175/BAMS-88-2-191.

Dee, D. P., and Coauthors, 2011: The ERA-Interim reanalysis: Configuration and performance of the data assimilation system. *Quart. J. Roy. Meteor. Soc.*, **137**, 553–597, doi:10.1002/qj.828.

Delanoë, J., A. Protat, J. Testud, D. Bouniol, A. J. Heymsfield, A. Bansemer, P. R. A. Brown, and R. M. Forbes, 2005: Statistical properties of the normalized ice particle size distribution. *J. Geophys. Res.*, **110**, D10201, doi:10.1029/2004JD005405.

Del Genio, A. D., M.-S. Yao, W. Kovari, and K. K.-W. Lo, 1996: A prognostic cloud water parameterization for global climate models. *J. Climate*, **9**, 270–304, doi:10.1175/1520-0442(1996)009<0270:APCWPF>2.0.CO;2.

——, W. Kovari, M.-S. Yao, and J. Jonas, 2005: Cumulus microphysics and climate sensitivity. *J. Climate*, **18**, 2376–2387, doi:10.1175/JCLI3413.1.

——, M.-S. Yao, and J. Jonas, 2007: Will moist convection be stronger in a warmer climate? *Geophys. Res. Lett.*, **34**, LI6703, doi:10.1029/2007GL030525.

——, J. Wu, A. Wolf, Y. Chen, M.-S. Yao, and D. Kim, 2015: Constraints on cumulus parameterization from simulations of observed MJO events. *J. Climate*, **28**, 6419–6442, doi:10.1175/JCLI-D-14-00832.1.

Donner, L. J., C. J. Seman, and R. S. Hemler, 2001: A cumulus parameterization including mass fluxes, convective vertical velocities, and mesoscale effects: Thermodynamic and hydrological aspects in a general circulation model. *J. Climate*, **14**, 3444–3463, doi:10.1175/1520-0442(2001)014<3444:ACPIMF>2.0.CO;2.

——, and Coauthors, 2011: The dynamical core, physical parameterizations, and basic simulation characteristics of the atmospheric component AM3 of the GFDL global coupled model CM3. *J. Climate*, **24**, 3484–3519, doi:10.1175/2011JCLI3955.1.

Emanuel, K. A., and M. Živković-Rothman, 1999: Development and evaluation of a convection scheme for use in climate models. *J. Atmos. Sci.*, **56**, 1766–1782, doi:10.1175/1520-0469(1999)056<1766:DAEOAC>2.0.CO;2.

Evans, K. F., and G. L. Stephens, 1995: Microwave radiative transfer through clouds composed of realistically shaped ice crystals. Part II: Remote sensing of ice clouds. *J. Atmos. Sci.*, **52**, 2058–2072, doi:10.1175/1520-0469(1995)052<2058:MRTTCC>2.0.CO;2.

——, J. R. Wang, P. E. Racette, G. M. Heymsfield, and L. Li, 2005: Ice cloud retrievals and analysis with the compact scanning submillimeter imaging radiometer and the cloud radar system during CRYSTAL FACE. *J. Appl. Meteor.*, **44**, 839–859, doi:10.1175/JAM2250.1.

Field, P. R., and A. J. Heymsfield, 2003: Aggregation and scaling of ice crystal size distributions. *J. Atmos. Sci.*, **60**, 544–560, doi:10.1175/1520-0469(2003)060<0544:AASOIC>2.0.CO;2.

Fontaine, E., A. Schwarzenboeck, J. Delanoë, W. Wobrock, D. Leroy, R. Dupuy, C. Gourbeyre, and A. Protat, 2014: Constraining mass–diameter relations from hydrometeor images and cloud radar reflectivities in tropical continental and oceanic convective anvils. *Atmos. Chem. Phys.*, **14**, 11 367–11 392, doi:10.5194/acp-14-11367-2014.

Fridlind, A. M., A. S. Ackerman, A. Grandin, F. Dezitter, M. Weber, J. W. Strapp, A. V. Korolev, and C. R. Williams, 2015: High ice water content at low radar reflectivity near deep convection—Part I: Consistency of in situ and remote-sensing observations with stratiform rain column simulations. *Atmos. Chem. Phys.*, **15**, 11 713–11 728, doi:10.5194/acp-15-11713-2015.

Giangrande, S. E., S. Collis, J. Straka, A. Protat, C. Williams, and S. Krueger, 2013: A summary of convective-core vertical velocity properties using ARM UHF wind profilers in Oklahoma. *J. Appl. Meteor. Climatol.*, **52**, 2278–2295, doi:10.1175/JAMC-D-12-0185.1.

Gregory, D., 2001: Estimation of entrainment rate in simple models of convective clouds. *Quart. J. Roy. Meteor. Soc.*, **127**, 53–72, doi:10.1002/qj.49712757104.

Hallett, J., 2003: Measurement in the atmosphere. *Handbook of Weather, Climate, and Water: Dynamics, Climate, Physical Meteorology, Weather Systems, and Measurements*, T. D. Potter and B. R. Colman, Eds., Wiley-Interscience, 711–720, doi:10.1002/0471721603.

Hartmann, D. L., M. E. Ockertbell, and M. L. Michelsen, 1992: The effect of cloud type on Earth's energy balance—Global analysis. *J. Climate*, **5**, 1281–1304, doi:10.1175/1520-0442(1992)005<1281:TEOCTO>2.0.CO;2.

Haynes, J. M., T. S. L'Ecuyer, G. L. Stephens, S. D. Miller, C. Mitrescu, N. B. Wood, and S. Tanelli, 2009: Rainfall retrieval over the ocean with spaceborne W-band radar. *J. Geophys. Res.*, **114**, D00A22, doi:10.1029/2008JD009973.

——, T. L'Ecuyer, D. Vane, G. Stephens, and D. Reinke, 2013: Level 2-C precipitation column algorithm product process description and interface control document. 17 pp. [Available online at http://www.cloudsat.cira.colostate.edu/data-products/level-2c/2c-precip-column.]

Heymsfield, A. J., 2007: On measurements of small ice particles in clouds. *Geophys. Res. Lett.*, **34**, L23812, doi:10.1029/2007GL030951.

——, A. Bansemer, P. R. Field, S. L. Durden, J. L. Stith, J. E. Dye, W. Hall, and C. A. Grainger, 2002: Observations and parameterizations of particle size distributions in deep tropical cirrus and stratiform precipitating clouds: Results from in situ observations in TRMM field campaigns. *J. Atmos. Sci.*, **59**, 3457–3491, doi:10.1175/1520-0469(2002)059<3457:OAPOPS>2.0.CO;2.

——, C. Schmitt, A. Bansemer, and C. H. Twohy, 2010: Improved representation of ice particle masses based on observations in natural clouds. *J. Atmos. Sci.*, **67**, 3303–3318, doi:10.1175/2010JAS3507.1.

——, ——, and ——, 2013: Ice cloud particle size distributions and pressure-dependent terminal velocities from in situ observations at temperatures from 0° to −86°C. *J. Atmos. Sci.*, **70**, 4123–4154, doi:10.1175/JAS-D-12-0124.1.

Heymsfield, G. M., L. Tian, A. J. Heymsfield, L. Li, and S. Guimond, 2010: Characteristics of deep tropical and subtropical convection from nadir-viewing high-altitude airborne Doppler radar. *J. Atmos. Sci.*, **67**, 285–308, doi:10.1175/2009JAS3132.1.

Jackson, R. C., and G. M. McFarquhar, 2014: An assessment of the impact of antishattering tips and artifact removal techniques on bulk cloud ice microphysical and optical properties measured by the 2D Cloud Probe. *J. Atmos. Oceanic Technol.*, **31**, 2131–2144, doi:10.1175/JTECH-D-14-00018.1.

——, and Coauthors, 2012: The dependence of ice microphysics on aerosol concentration in Arctic mixed-phase stratus clouds during ISDAC and M-PACE. *J. Geophys. Res.*, **117**, D15207, doi:10.1029/2012JD017668.

——, G. M. McFarquhar, A. M. Fridlind, and R. Atlas, 2015: The dependence of cirrus gamma size distributions expressed as volumes in N_0-λ-μ phase space and bulk cloud properties on environmental conditions: Results from the Small Ice Particles in Cirrus Experiment (SPARTICUS). *J. Geophys. Res. Atmos.*, **120**, 10 351–10 377, doi:10.1002/2015JD023492.

Jensen, M., and Coauthors, 2016: The Midlatitude Continental Convective Clouds Experiment (MC3E). *Bull. Amer. Meteor. Soc.*, **97**, 1667–1686, doi:10.1175/BAMS-D-14-00228.1.

Jiang, J. H., and Coauthors, 2012: Evaluation of cloud and water vapor simulations in CMIP5 climate models using NASA "A-Train" satellite observations. *J. Geophys. Res.*, **117**, D14105, doi:10.1029/2011JD017237.

Kim, D., A. D. Del Genio, and M.-S. Yao, 2013: Moist convection scheme in Model E2. 9 pp. [Available online at https://arxiv.org/abs/1312.7496.]

Korolev, A., E. Emery, J. W. Strapp, S. G. Cober, G. A. Isaac, M. Wasey, and D. Marcotte, 2011: Small ice particles in tropospheric clouds: Fact or artifact? *Bull. Amer. Meteor. Soc.*, **92**, 967–973, doi:10.1175/2010BAMS3141.1.

——, ——, and K. Creelman, 2013: Modification and tests of particle probe tips to mitigate effects of ice shattering. *J. Atmos. Oceanic Technol.*, **30**, 690–708, doi:10.1175/JTECH-D-12-00142.1.

Lawson, R. P., 2011: Effects of ice particles shattering on the 2D-S probe. *Atmos. Meas. Tech.*, **4**, 1361–1381, doi:10.5194/amt-4-1361-2011.

——, D. O'Connor, P. Zmarzly, K. Weaver, B. Baker, Q. Mo, and H. Jonsson, 2006: The 2D-S (Stereo) Probe: Design and preliminary tests of a new airborne, high-speed, high-resolution particle imaging probe. *J. Atmos. Oceanic Technol.*, **23**, 1462–1477, doi:10.1175/JTECH1927.1.

——, E. Jensen, D. L. Mitchell, B. Baker, Q. Mo, and B. Pilson, 2010: Microphysical and radiative properties of tropical clouds investigated in TC4 and NAMMA. *J. Geophys. Res.*, **115**, D00J08, doi:10.1029/2009JD013017.

Leroy, D., and Coauthors, 2015: HAIC/HIWC Field Campaign—Specific findings on PSD microphysics in high IWC regions from in situ measurements: Median mass diameters, particle size distribution characteristics and ice crystal shapes. SAE Tech. Paper 2015-01-2087, 8 pp., doi:10.4271/2015-01-2087.

Locatelli, J. D., and P. V. Hobbs, 1974: Fall speeds and masses of solid precipitation particles. *J. Geophys. Res.*, **79**, 2185–2197, doi:10.1029/JC079i015p02185.

Luo, Z., and W. B. Rossow, 2004: Characterizing tropical cirrus life cycle, evolution, and interaction with upper-tropospheric water vapor using Lagrangian trajectory analysis of satellite observations. *J. Climate*, **17**, 4541–4563, doi:10.1175/3222.1.

Mace, J., E. Jensen, G. McFarquhar, J. Comstock, T. Ackerman, D. Mitchell, X. Liu, and T. Garrett, 2009: SPARTICUS—Small Particles in Cirrus Science and Operations Plan. ARM Program, 15 pp. [Available online at https://www.arm.gov/publications/programdocs/doe-sc-arm-10-003.pdf.]

Marshall, J. S., and W. M. Palmer, 1948: The distribution of raindrops with size. *J. Meteor.*, **5**, 165–166, doi:10.1175/1520-0469(1948)005<0165:TDORWS>2.0.CO;2.

Mauritsen, T., and B. Stevens, 2015: Missing iris effect as a possible cause of muted hydrological change and high climate sensitivity in models. *Nat. Geosci.*, **8**, 346–351, doi:10.1038/ngeo2414.

——, and Coauthors, 2012: Tuning the climate of a global model. *J. Adv. Model. Earth Syst.*, **4**, M00A01, doi:10.1029/2012MS000154.

McFarquhar, G. M., and R. A. Black, 2004: Observations of particle size and phase in tropical cyclones: Implications for mesoscale modeling of microphysical processes. *J. Atmos. Sci.*, **61**, 422–439, doi:10.1175/1520-0469(2004)061<0422:OOPSAP>2.0.CO;2.

——, M. S. Timlin, R. M. Rauber, B. F. Jewett, J. A. Grim, and D. P. Jorgensen, 2007: Vertical variability of cloud hydrometeors in the stratiform region of mesoscale convective systems and bow echoes. *Mon. Wea. Rev.*, **135**, 3405–3428, doi:10.1175/MWR3444.1.

——, T. Hsieh, M. Freer, J. Mascio, and B. F. Jewett, 2015: The characterization of ice hydrometeor gamma size distributions as volumes in N_0-μ-λ phase space: Implications for microphysical process modeling. *J. Atmos. Sci.*, **72**, 892–909, doi:10.1175/JAS-D-14-0011.1.

Mitchell, D. L., S. Mishra, and R. P. Lawson, 2011: Representing the ice fall speed in climate models: Results from Tropical Composition, Cloud and Climate Coupling (TC4) and the Indirect and Semi-Direct Aerosol Campaign (ISDAC). *J. Geophys. Res.*, **116**, D00T03, doi:10.1029/2010JD015433.

Muhlbauer, A., T. P. Ackerman, J. M. Comstock, G. S. Diskin, S. M. Evans, R. P. Lawson, and R. T. Marchand, 2014: Impact of large-scale dynamics on the microphysical properties of midlatitude cirrus. *J. Geophys. Res. Atmos.*, **119**, 3976–3996, doi:10.1002/2013JD020035.

Protat, A., J. Delanoë, E. J. O'Connor, and T. S. L'Ecuyer, 2010: The evaluation of *CloudSat* and *CALIPSO* ice microphysical products using ground-based cloud radar and lidar observations. *J. Atmos. Oceanic Technol.*, **27**, 793–810, doi:10.1175/2009JTECHA1397.1.

Rotstayn, L. D., 2000: On the "tuning" of autoconversion parameterizations in climate models. *J. Geophys. Res.*, **105**, 15 495–15 507, doi:10.1029/2000JD900129.

Sanderson, B. M., C. Piani, W. J. Ingram, D. A. Stone, and M. R. Allen, 2008: Towards constraining climate sensitivity by linear analysis of feedback patterns in thousands of perturbed-physics GCM simulations. *Climate Dyn.*, **30**, 175–190, doi:10.1007/s00382-007-0280-7.

Schmidt, G. A., and Coauthors, 2014: Configuration and assessment of the GISS Model E2 contributions to the CMIP5 archive. *J. Adv. Model. Earth Syst.*, **6**, 141–184, doi:10.1002/2013MS000265.

Schumacher, C., and R. A. Houze Jr., 2003: Stratiform rain in the tropics as seen by the TRMM Precipitation Radar. *J. Climate*, **16**, 1739–1756, doi:10.1175/1520-0442(2003)016<1739:SRITTA>2.0.CO;2.

Scott, S. G., T. P. Bui, K. R. Chan, and S. W. Bowen, 1990: The meteorological measurement system on the NASA ER-2

aircraft. *J. Atmos. Oceanic Technol.*, **7**, 525–540, doi:10.1175/1520-0426(1990)007<0525:TMMSOT>2.0.CO;2.

Song, X., and G. J. Zhang, 2011: Microphysics parameterization for convective clouds in a global climate model: Description and single-column model tests. *J. Geophys. Res.*, **116**, D02201, doi:10.1029/2010JD014833.

Stanfield, R. E., X. Dong, B. Xi, A. Kennedy, A. D. Del Genio, P. Minnis, and J. H. Jiang, 2014: Assessment of NASA GISS CMIP5 and post-CMIP5 simulated clouds and TOA radiation budgets using satellite observations. *J. Climate*, **27**, 4189–4208, doi:10.1175/JCLI-D-13-00558.1.

Stephens, G. L., 2005: Cloud feedbacks in the climate system: A critical review. *J. Climate*, **18**, 237–273, doi:10.1175/JCLI-3243.1.

——, and Coauthors, 2002: The *CloudSat* mission and the A-Train: A new dimension of space-based observations of clouds and precipitation. *Bull. Amer. Meteor. Soc.*, **83**, 1771–1790, doi:10.1175/BAMS-83-12-1771.

Storer, R. L., G. J. Zhang, and X. Song, 2015: Effects of convective microphysics parameterization on large-scale cloud hydrological and radiative budget in tropical and midlatitude convective regions. *J. Climate*, **28**, 9277–9297, doi:10.1175/JCLI-D-15-0064.1.

Su, H., and Coauthors, 2013: Diagnosis of regime-dependent cloud simulation errors in CMIP5 models using ''A-Train'' satellite observations and reanalysis data. *J. Geophys. Res. Atmos.*, **118**, 2762–2780, doi:10.1029/2012JD018575.

Testud, J., S. Oury, R. A. Black, P. Amayenc, and X. Dou, 2001: The concept of ''normalized'' distribution to describe raindrop spectra: A tool for cloud physics and cloud remote sensing. *J. Appl. Meteor. Climatol.*, **40**, 1118–1140, doi:10.1175/1520-0450(2001)040<1118:TCONDT>2.0.CO;2.

Toon, O. B., and Coauthors, 2010: Planning, implementation, and first results of the Tropical Composition, Cloud and Climate Coupling Experiment (TC4). *J. Geophys. Res.*, **115**, D00J04, doi:10.1029/2009JD013073.

Varble, A., and Coauthors, 2011: Evaluation of cloud-resolving model intercomparison simulations using TWP-ICE observations: Precipitation and cloud structure. *J. Geophys. Res.*, **116**, D12206, doi:10.1029/2010JD015180.

——, and Coauthors, 2014: Evaluation of cloud-resolving and limited area model intercomparison simulations using TWP-ICE observations:1. Deep convective updraft properties. *J. Geophys. Res. Atmos.*, **119**, 13 891–13 918, doi:10.1002/2013JD021371.

Waliser, D., and Coauthors, 2009: Cloud ice: A climate model challenge with signs and expectations of progress. *J. Geophys. Res.*, **114**, D00A21, doi:10.1029/2008JD010015.

Waters, J. W., and Coauthors, 2006: The Earth Observing System Microwave Limb Sounder (EOS MLS) on the *Aura* satellite. *IEEE Trans. Geosci. Remote Sens.*, **44**, 1075–1092.

Woods, C. P., D. E. Waliser, J.-L. Li, R. T. Austin, G. L. Stephens, and D. G. Vane, 2008: Evaluating *CloudSat* ice water content retrievals using a cloud-resolving model: Sensitivities to frozen particle properties. *J. Geophys. Res.*, **113**, D00A11, doi:10.1029/2008JD009941.

Wu, D. L., and Coauthors, 2008: Validation of the *Aura* MLS cloud ice water content measurements. *J. Geophys. Res.*, **113**, D15S10, doi:10.1029/2007JD008931.

——, and Coauthors, 2009: Comparisons of global cloud ice from MLS, *CloudSat*, and correlative data sets. *J. Geophys. Res.*, **114**, D00A24, doi:10.1029/2008JD009946.

Wu, W., and G. M. McFarquhar, 2016: On the impacts of different definitions of maximum dimension for nonspherical particles recorded by 2D imaging probes. *J. Atmos. Oceanic Technol.*, **33**, 1057–1072, doi:10.1175/JTECH-D-15-0177.1.

Zelinka, M. D., S. A. Klein, and D. L. Hartmann, 2012a: Computing and partitioning cloud feedbacks using cloud property histograms. Part I: Cloud radiative kernels. *J. Climate*, **25**, 3715–3735, doi:10.1175/JCLI-D-11-00248.1.

——, ——, and ——, 2012b: Computing and partitioning cloud feedbacks using cloud property histograms. Part II: Attribution to changes in cloud amount, altitude, and optical depth. *J. Climate*, **25**, 3736–3754, doi:10.1175/JCLI-D-11-00249.1.

Zhang, G. J., and N. A. McFarlane, 1995: Sensitivity of climate simulations to the parameterization of cumulus convection in the Canadian Climate Centre general circulation model. *Atmos.–Ocean*, **33**, 407–446, doi:10.1080/07055900.1995.9649539.

Zhang, K., X. Liu, M. Wang, J. M. Comstock, D. L. Mitchell, S. Mishra, and G. G. Mace, 2013: Evaluating and constraining ice cloud parameterizations in CAM5 using aircraft measurements from the SPARTICUS campaign. *Atmos. Chem. Phys.*, **13**, 4963–4982, doi:10.5194/acp-13-4963-2013.

Zhao, M., 2014: An investigation of the connections among convection, clouds, and climate sensitivity in a global climate model. *J. Climate*, **27**, 1845–1862, doi:10.1175/JCLI-D-13-00145.1.

Zipser, E. J., and Coauthors, 2009: The Saharan air layer and the fate of African easterly waves—NASA's AMMA field study of tropical cyclogenesis. *Bull. Amer. Meteor. Soc.*, **90**, 1137–1156, doi:10.1175/2009BAMS2728.1.